# The microtubule-nucleating factor MACERATOR tethers AUGMIN7 to microtubules and governs phragmoplast architecture

Sharol Schmidt-Marcec (D, 1, 4 Alyssa Parish (D, 1, 4 Tetyana Smertenko (D, 1 Matthew Hickey (D, 1 Bernard M.A.G. Piette (D) and Andrei Smertenko (D) 1, \*

- I Institute of Biological Chemistry, Washington State University, Pullman, Washington 99164, USA
- 2 Department of Mathematics, Durham University, Durham HD1 3LE, UK

The author responsible for distribution of materials integral to the findings presented in this article in accordance with the policy described in the Instructions for Authors (https://academic.oup.com/plcell/pages/General-Instructions) is: Andrei Smertenko (andrei.smertenko@wsu.edu).

#### Abstract

The plant cytokinetic microtubule array, called the phragmoplast, exhibits higher microtubule dynamics in its center (midzone) than at the periphery (distal zone). This behavior is known as the axial asymmetry. Despite being a major characteristic of the phragmoplast, little is known about regulators of this phenomenon. Here we address the role of microtubule nucleation in axial asymmetry by characterizing MACERATOR (MACET) proteins in *Arabidopsis thaliana* and *Nicotiana benthamiana* with a combination of genetic, biochemical, and live-cell imaging assays, using photo-convertible microtubule probes, and modeling. MACET paralogs accumulate at the shrinking microtubule ends and decrease the tubulin OFF rate. Loss of MACET4 and MACET5 function abrogates axial asymmetry by suppressing microtubule dynamicity in the midzone. MACET4 also narrows the microtubule nucleation angle at the phragmoplast leading edge and functions as a microtubule tethering factor for AUGMIN COMPLEX SUBUNIT 7 (AUG7). The *macet4 macet5* double mutant shows diminished clustering of AUG7 in the phragmoplast distal zone. Knockout of *AUG7* does not affect MACET4 localization, axial asymmetry, or microtubule nucleation angle, but increases phragmoplast length and slows down phragmoplast expansion. The *mce4-1 mce5 aug7-1* triple knockout is not viable. Experimental data and modeling demonstrate that microtubule nucleation factors regulate phragmoplast architecture and axial asymmetry directly by generating new microtubules and indirectly by modulating the abundance of free tubulin.

### Introduction

Land plants partition cellular contents between daughter cells during cytokinesis via the cell plate, a membrane compartment containing callose and other oligosaccharides. Assembly of the cell plate is facilitated by a plant-specific polarized secretory module known as the phragmoplast (Bajer 1968; Lipka et al. 2015). The phragmoplast consists of microtubules, actin filaments, cytokinetic vesicles, and numerous associated proteins. Microtubules provide a scaffold for cell plate biosynthesis as well as delivery tracks for cytokinetic vesicles carrying building materials to the cell plate construction site at the central part of the phragmoplast, called the

midzone. Typically, the phragmoplast starts as a disk from the remnants of the anaphase spindle between daughter nuclei (Asada et al. 1991; Wasteneys 2002). As cells are generally wider than the phragmoplast diameter, the phragmoplast initially lacks direct contact with the parental cell wall. Completing cell plate biosynthesis requires centrifugal phragmoplast expansion from the cell center toward the parental cell wall (Wasteneys 2002). Phragmoplast expansion depends on microtubule nucleation and dynamics. For example, phragmoplast microtubules in tobacco (*Nicotiana tabacum*) and Virginia spiderwort (*Tradescantia virginiana*) are twice as dynamic as interphase microtubules (Hush et al. 1994;

<sup>\*</sup>Author for correspondence: andrei.smertenko@wsu.edu (A.S.)

<sup>&</sup>lt;sup>†</sup>These authors contributed equally to this work.

### IN A NUTSHELL

**Background:** The success of many cellular programs depends on asymmetry, resulting from a shift of cellular components from an even to uneven distribution. Understanding the rules of cellular asymmetry requires information about structural blocks and their behavior under specific contexts. We harnessed cell division as a model system to explore cellular asymmetry. Cells in land plants divide via the formation of a cell plate, a partition made from membranes and oligosaccharides. The cell plate is constructed by an asymmetrical structure known as the phragmoplast, whose structure is maintained by microtubules, 25-nm thick tubes built from the protein tubulin. Microtubules govern phragmoplast asymmetry through three types of behavior: nucleation (birth of a new microtubule), growth, and shrinkage. Transition between these behaviors is controlled by tubulin availability: higher tubulin abundance promotes microtubule polymerization, whereas low tubulin abundance triggers depolymerization. Cells contain a fixed amount of tubulin, meaning that microtubule polymerization causes depletion of tubulin, leading to depolymerization and vice versa.

Question: What is the role of microtubule nucleation in phragmoplast asymmetry?

**Findings:** We analyzed the *Arabidopsis thaliana* MACERATOR (MACET) family comprising seven plant-specific microtubule-nucleating proteins. Mutants lacking MACET4 and MACET5 function (*mce4-1 mce5*) showed defective phragmoplast asymmetry and morphology caused by a greater angle of branched microtubule nucleation. MACET4 interacts with the plant-specific microtubule nucleation factor AUGMIN7. Simultaneous mutation of *MACET4*, *MACET5*, and *AUGMIN7*, causes plant lethality. A computational analysis revealed that microtubule nucleation by MACET depletes tubulin, leading to destabilization of phragmoplast microtubules. Hence, assembly factors contribute to cellular asymmetry directly by defining the architecture of cellular structures and indirectly by the controlling abundance of their building blocks.

**Next steps:** Proteins that cooperate with MACET need to be identified and their functions characterized. Determining the rules of cellular asymmetry would advance understanding of life and enable engineering of living systems.

Smertenko et al. 2011) and suppressing microtubule dynamics with taxol disrupts phragmoplast expansion (Yasuhara et al. 1993).

Microtubule forms by oligomerization of tubulin through nucleation. Nucleation can be spontaneous when the rate of tubulin association with existing tubulin oligomers (the ON rate) is greater than the rate of tubulin dissociation from the oligomers (the OFF rate) (Roostalu et al. 2015; Wieczorek et al. 2015). The minimal concentration of tubulin that supports spontaneous nucleation is termed "critical concentration" (Obermann et al. 1990). However, the concentration of tubulin in a cell is thought to be below this critical concentration and microtubule nucleation must, therefore, be facilitated by nucleation factors. By definition, a microtubule nucleation factor promotes tubulin polymerization under conditions when spontaneous nucleation is impossible. At above critical concentrations of tubulin in vitro, the nucleation factors increase the nucleation rate. A nucleation factor can increase the ON rate or decrease the OFF rate as well as define the location of the nucleation events (Roostalu et al. 2015; Wieczorek et al. 2015).

The most common microtubule nucleation factor is the  $\gamma$ -tubulin ring complex ( $\gamma$ -TuRC) comprising six subunits, GCP1 to GCP6, with  $\gamma$ -tubulin being  $\gamma$ -TUBULIN RING COMPLEX PROTEIN 1 (GCP1) (Hashimoto 2013).  $\gamma$ -TuRC can be cytoplasmic or associate with extant microtubules (Murata et al. 2005). Nucleation on the lattice of existing

microtubules results in a "branched" nucleation event. The average angle of branched microtubule nucleation during interphase is 40° (Walia et al. 2014).  $\gamma$ -TuRC can interact with other proteins, the most common of which is the augmin complex comprising eight subunits (AUG1 to AUG8) (Liu et al. 2014; Song et al. 2018). Among known augmin complex functions are the tethering of  $\gamma$ -TuRC to microtubules and maintaining the angle of branched microtubule nucleation (Alfaro-Aco et al. 2020). In plants, the augmin complex determines the frequency rather than the angle of branched nucleation events (Liu et al. 2014) whereas the  $\gamma$ -TuRC-interacting protein GCP-WD (previously named NEURAL PRECURSOR CELL EXPRESSED [NEDD1]) determines the angle of the branched nucleation (Walia et al. 2014).

Every microtubule has two ends: the minus end that is frequently attached to  $\gamma$ -TuRC; the plus end that undergoes polymerization or depolymerization through addition or loss of tubulin monomers (Akhmanova and Steinmetz 2008). The probability of transitioning between polymerization and depolymerization states is determined by the availability of free tubulin (VanBuren et al. 2005). Depletion of free tubulin in the course of microtubule polymerization eventually causes a drop in the ON rate leading to catastrophe or transition from polymerization to depolymerization. Conversely, depolymerization releases free tubulin, increasing the tubulin pool size, and thus promoting polymerization by

increasing the ON rate. These transitions cause oscillations in the abundance of microtubule polymers (Obermann et al. 1990). Microtubules can also be in a stable state in which they neither grow nor shrink (Akhmanova and Steinmetz 2008). The stable state is common for those phragmoplast microtubules that form attachment to the cell plate assembly matrix (Austin et al. 2005).

The expanding phragmoplast can be subdivided into three regions according to microtubule behavior: (1) the leading zone where the dominant events are microtubule nucleation and growth; (2) the transition zone containing both dynamic and stable microtubules (Austin et al. 2005; Murata et al. 2013); and (3) the lagging zone that is dominated by microdepolymerization (Smertenko et Microtubules nucleate at the phragmoplast outer regions, known as the distal zones. As a consequence, most (over 90%) microtubule plus-ends face the cell plate, with minus ends facing the nucleus (Euteneuer and McIntosh 1980). Branched nucleation events occur at the leading zone (Murata et al. 2013). Microtubules nucleated through this mechanism become gradually incorporated into the main body of the phragmoplast.

Microtubule dynamics in the phragmoplast exhibit two types of asymmetry. Lateral asymmetry encompasses microtubule polymerization in the leading zone and microtubule depolymerization in the lagging zone (Seguié-Simarro et al. 2008; Murata et al. 2013). Axial asymmetry is generated by faster microtubule dynamics in the midzone than in the distal zone (Smertenko et al. 2011). The rules and mechanisms governing phragmoplast asymmetry remain poorly understood. According to our published modeling work, microtubule polarity is essential but not sufficient for axial asymmetry. We also predicted that microtubule nucleation plays a key role in axial asymmetry (Smertenko et al. 2011). However, experimental testing of this hypothesis was hindered by the lethality, sterility, or severe developmental defects seen in the mutants of  $\gamma$ -TuRC components. We recently showed that the plant-specific protein MACERATOR4 (MACET4, also named CORTICAL MICROTUBULE DISORDERING4 [CORD4]) promotes microtubule nucleation in vitro at subcritical concentrations of tubulin and localizes to microtubule-nucleation sites in vivo (Schmidt and Smertenko 2019). During cytokinesis, MACET4 localizes at the phragmoplast distal zone (Schmidt and Smertenko 2016, 2019; Sasaki et al. 2019). The knockout of MACET4 in the mce4-1 mutant increases phragmoplast length and this phenotype can be complemented by MACET4-GFP encoding a fusion between MACET4 and the green fluorescent protein (GFP) under control of MACET4 promoter (Schmidt and Smertenko 2019). The double knockout of MACET4 and MACET5 (also named CORD5) slows down phragmoplast expansion, increases phragmoplast length, decreases the angle of the phragmoplast leading edge and root length (Sasaki et al. 2019). This phenotype can be rescued by the transgenic expression of MACET4-GFP.

Aside from microtubule nucleation, two additional models have been proposed to explain the mechanism of MACET

activity. First, destabilization of microtubules by disrupting association of microtubules with the plasma membrane (shown for MACET1 [also named CORD1]; Sasaki et al. 2017). Second, destabilization of microtubules by tethering KATANIN to the microtubule lattice (shown for MACET4; Sasaki et al. 2019). In this study, we compared the effects of seven MACET paralogs from Arabidopsis (Arabidopsis thaliana) on microtubule dynamics and showed that all proteins decrease the tubulin OFF rate. Promoter reporter constructs demonstrated the overlapping expression pattern of individual MACET genes in meristems, reproductive organs, and in embryos, but a lack of promoter activity in differentiated vegetative tissues. We analyzed cytokinesis in the mce4-1 mce5 double mutant using the tubulin probes mNeonGreen-TuB2 (a fusion between the fluorescent protein mNeonGreen and β2 tubulin) and EosFP-TuB2, identified and characterized MACET4 interactors, modeled the role of MACET in phragmoplast microtubule dynamics, and experimentally verified the predictions of the model. Our work demonstrates that MACET proteins regulate the angle of branching microtubule nucleation, interact with microtubule nucleation complexes, maintain axial asymmetry, and govern the ratio between monomeric and polymeric tubulin during cytokinesis.

### **Results**

#### MACET proteins decrease the tubulin OFF rate

The Arabidopsis genome has seven MACET/CORD paralogs (Sasaki et al. 2017; Schmidt and Smertenko 2019). The biochemical activity was only characterized for MACET4 (Schmidt and Smertenko 2019). Here we analyzed the activity of other paralogs. While MACET4 was previously published as being soluble, all other paralogs yielded insoluble recombinant protein in Escherichia coli under buffer conditions compatible with microtubule dynamics assays. As an alternative, we compared microtubule behavior in Nicotiana benthamiana leaf pavement cells ectopically expressing each paralog gene under the control of a strong constitutive promoter. Our experimental design included analysis of both N- and C-terminal GFP fusions to mitigate the potential influence of GFP on protein activity. We used GFP-TuB6 as a negative control because this construct exhibits no discernible effect on microtubule dynamics (Abe and Hashimoto 2005); we used MACET4 as a positive control because this protein was extensively characterized in vivo and in vitro (Schmidt and Smertenko 2019). We recorded time lapse images of three to six representative cells per construct with similar intensity for GFP fluorescence.

We color-coded growing and shrinking microtubule ends from the time series (Fig. 1A). The length of colored extensions represents changes of microtubule length during five consecutive frames corresponding to time intervals of 18 to 19 s. Microtubules in control cells expressing *GFP-TuB6* contained green and magenta ends indicating polymerization and depolymerization events, respectively (Fig. 1A).

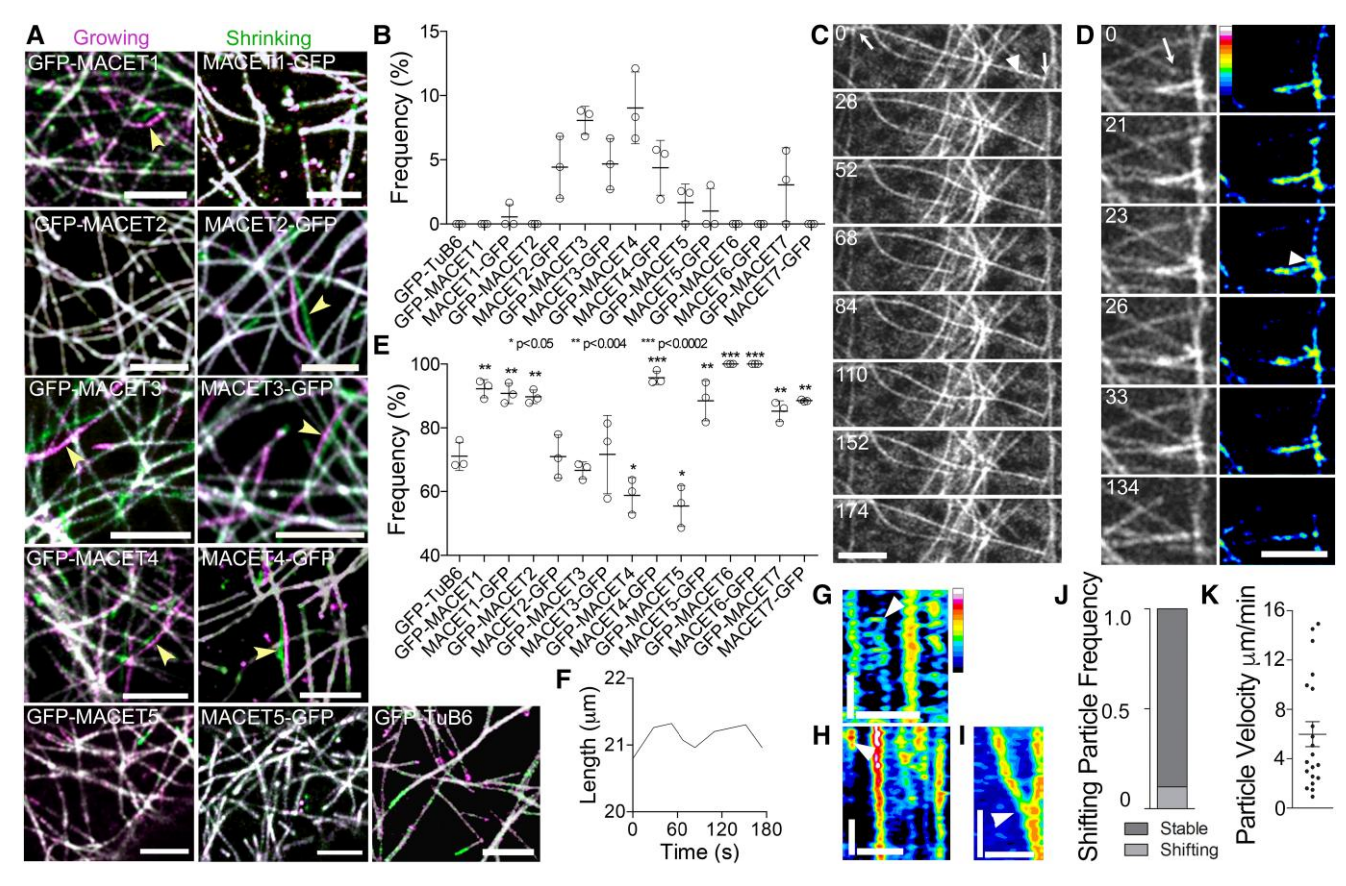


**Figure 1.** Effect of MACET paralogs from Arabidopsis on microtubule behavior in *N. benthamiana* leaf pavement cells. **A)** Frame subtraction images showing growing microtubule ends in red and shrinking microtubule ends in magenta. Arrowheads indicate wavering. Scale bars, 5  $\mu$ m. The time difference between the frames is 18.32 s for control and MACET4, 18 s for MACET1 and MACET2, 18.84 s for MACET5 and MACET3. **B)** Frequency of stable microtubule ends in cells expressing each *MACET-GFP* or *GFP-MACET* fusion construct. Asterisks denote statistical difference compared to the *GFP-TuB6* control (n = 5 cells per each construct). **C)** Time lapse images of a wavering microtubule in a cell expressing *GFP-MACET4*. Numbers indicate relative time in s. Scale bar, 5  $\mu$ m. Arrowhead points to the wavering microtubule. Arrows indicate the distance measured in **F. D)** MACET4 inhibits collision-induced catastrophe and accumulates at the end of microtubule upon collision. Numbers indicate relative time in s. The heatmap shows signal intensity. The arrow points to the tip of a growing microtubule and the arrowhead shows accumulation of MACET4-GFP at the point of collision. Scale bar, 5  $\mu$ m. **E)** Frequency of wavering microtubules in cells expressing each *MACET-GFP* or *GFP-MACET* fusion construct (n = 5 cells per construct). **F)** Length of the wavering microtubule shown in panel **C** measured between two arrows. **G to 1)** Kymographs derived from cells expressing *GFP-MACET1* showing the behavior of puncta. The arrowheads point association of puncta with microtubules (**G**), dissociation (**H**), diffusion along a microtubule and fusion (**1)**. Horizontal scale bar, 2  $\mu$ m, vertical scale bar, 60 s. **J)** Frequency of diffusing particles (n = 182 tracked puncta in 37 kymographs from five different cells). **K)** Diffusion velocity of puncta (n = 20 moving puncta in 37 kymographs from five different cells).

We did not detect colored extensions in cells expressing MACET6; for the other MACETs, we detected short colored extensions (Fig. 1A; Supplementary Fig. S1 B). We counted the frequency of non-dynamic (noncolored) ends for each construct relative to cells expressing GFP-TuB6 and observed a higher frequency of nondynamic microtubules in cells expressing MACET1, MACET2, MACET4, MACET5, or MACET7 (Fig. 1B; Table 1).

Another phenotype caused by ectopic expression of GFP-MACET1, MACET2-GFP, GFP-MACET3, MACET3-GFP, GFP-MACET4, MACET4-GFP, and GFP-MACET7 was coloration along microtubules (Fig. 1A; Supplementary Fig. S1B; arrowheads). These instances correspond to lateral displacement events known as "wavering", as shown in

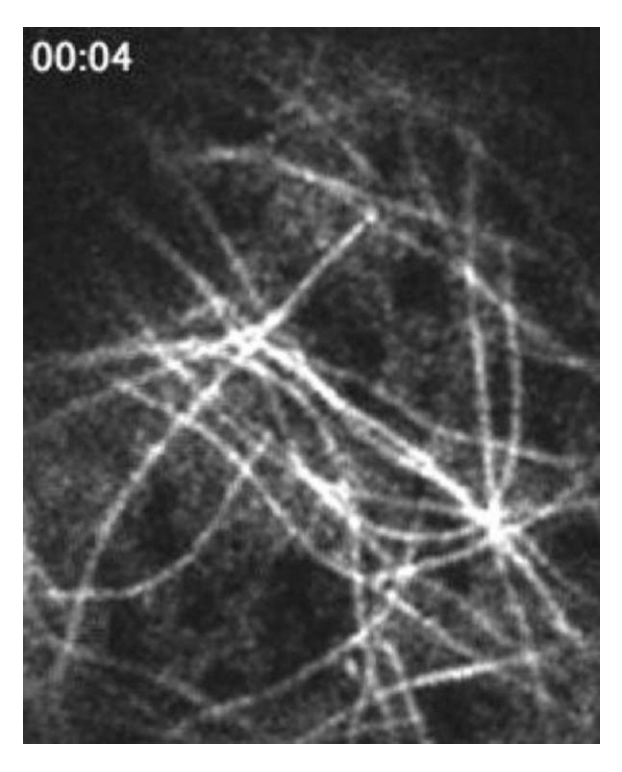
Fig. 1C for *GFP-MACET4* and in Supplementary Fig. S1 C for *GFP-MACET1*. The frequency of wavering microtubules varied between 0% and 9% (Fig. 1E). In each case, wavering was accompanied by an increase of microtubule length (Fig. 1F; Supplementary Fig. S1 D). A representative example of a wavering event is shown in Video 1 that occurs upon one microtubule encountering other microtubules. In some instances, an encounter triggered the accumulation of MACET at the contact site, followed by inhibition of microtubule depolymerization (Fig. 1D; Video 2). Only cells expressing TuB6 or MACET6 displayed no wavering.

Some coloration appeared along nonwavering microtubules in cells expressing *GFP-MACET1*, suggesting lateral diffusion or dissociation of the GFP signal from microtubules.

Table 1. Characterization of the MACET protein family

Protein	Expression domain	Suppresses microtubule dynamics <sup>a</sup>	Induces wavering <sup>a</sup>	Polymerization rate <sup>a</sup>	Depolymerization rate <sup>a</sup>
MACET1	Vascular	Yes	Yes	Slower	Slower
MACET2	Generative organs	Yes	Yes	Slower	Faster
MACET3	Generative organs and stems	No	Yes	Slower	Slower
MACET4	Meristems and young organs	Yes	Yes	Faster	Slower
MACET5	Meristems and young organs	Yes	Yes	ND	Slower
MACET6	Pollen	Yes	No	ND	ND
MACET7	Root and shoot apical meristems	Yes	Yes	Slower	Slower

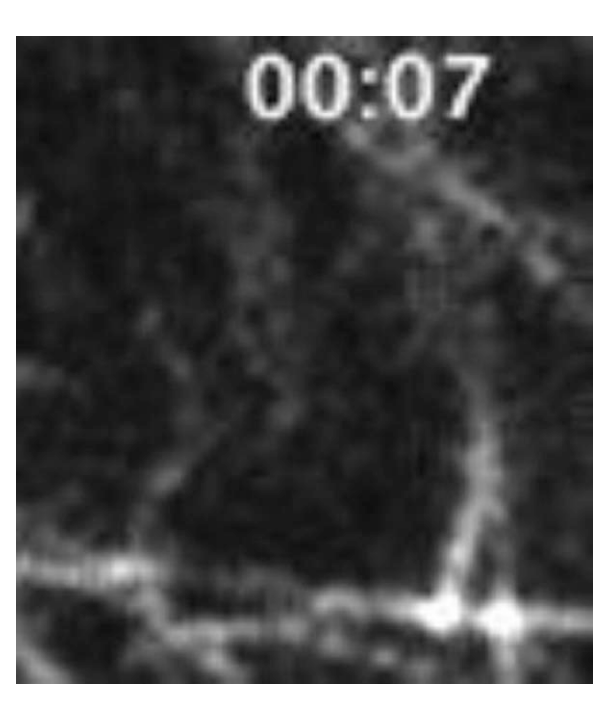
<sup>&</sup>lt;sup>a</sup>Derived from ectopic expression assays in N. benthamiana leaf pavement cells. A 35S:GFP-TuB6 construct was used as control; ND, not determined due to low frequency of corresponding events.



**Video 1.** A representative example of a microtubule wavering upon encountering another microtubule in a cell expressing *GFP-MACET4*. This example shows that instead of switching to catastrophe, a microtubule continues to push against another microtubule.

Tracking individual GFP puncta revealed the association of puncta with microtubules (Fig. 1G), their dissociation from microtubules (Fig. 1H), and their lateral diffusion followed by fusion with other puncta (Fig. 1I). We determined that 9% of puncta are mobile, with an average velocity of 6.39  $\mu$ m/min (Fig. 1, J and K). We did not observe moving puncta with other MACETs.

Co-localization with mCherry–TuA5 (a fusion between mCherry and alpha-tubulin 5) showed that all microtubules in the cells are labeled by the corresponding fusion between MACET and GFP. Two representative examples are shown for MACET1-GFP and MACET6–GFP in Supplementary Fig. S1 F. Kymographs of all MACET-GFP fusions demonstrated persistent labeling of microtubule ends during polymerization or depolymerization events (Fig. 2, A and B). Therefore, the GFP



**Video 2.** An example of elongating microtubule encountering another microtubule in a cell expressing *MACET4-GFP*. MACET4-GFP accumulates at the collision site with another microtubule. Despite losing a fragment from the end, the microtubule remains stable.

signal of the MACET-GFP fusions can be used to trace microtubule length. All proteins accumulated at depolymerizing microtubule ends, forming a bright "cap" with the exception of MACET6 for which we did not observe depolymerizing ends under our experimental conditions (Fig. 2B; Supplementary Fig. S1 B). The intensity of GFP signal at the depolymerizing ends was twice as high than along the microtubule lattice. We also observed occasional loss and re-appearance of the GFP cap from the depolymerizing ends, as exemplified for GFP-MACET1 in Supplementary Fig. S1 G.

Kymograph analysis demonstrated a slower microtubule depolymerization rate in cells ectopically expressing all MACET constructs, with the exception of MACET2 (Fig. 2C), although GFP-MACET2 decreased the frequency of dynamic microtubule ends (Table 1). A faster depolymerization rate in cells expressing MACET5-GFP was accompanied

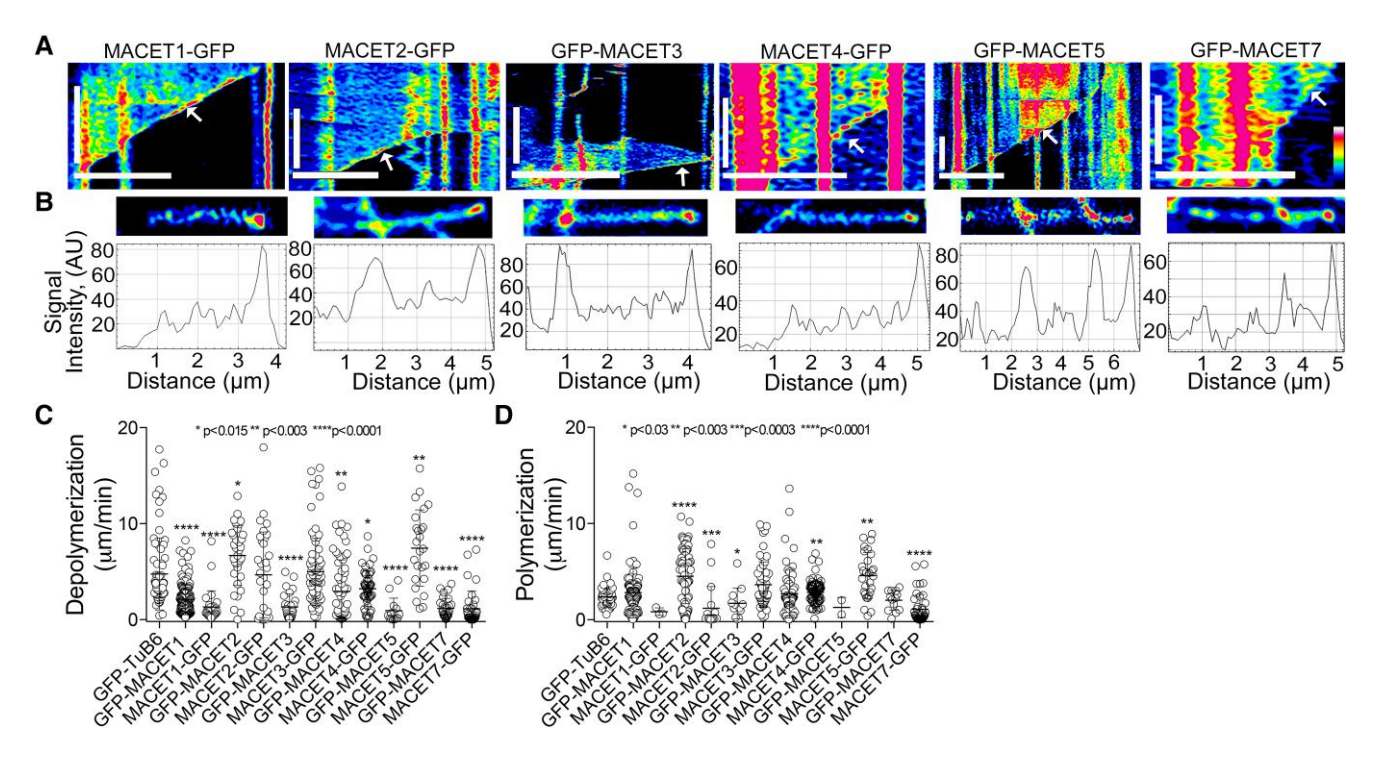


**Figure 2.** MACET paralogs accumulate at the shrinking ends and alter microtubule dynamics in *N. benthamiana* leaf pavement cells. **A)** Representative kymographs derived from the GFP signal at depolymerizing microtubule ends (arrows). Horizontal scale bar, 2 min, vertical scale bar, 5  $\mu$ m. **B)** Representative images of shrinking microtubules and corresponding fluorescence signal intensity plots below showing GFP signal enrichment on the ends. There is a brighter signal at the crossovers with other microtubules. **C and D)** Microtubule depolymerization (**C)** and polymerization (**D)** rates in cells expressing each *MACET-GFP* or *GFP-MACET* fusion construct. The *P*-values were determined by an unpaired *t*-test compared to *GFP-TuB6* control (12 < n < 135 data points measured in five cells per each sample).

by a higher frequency of stable ends (Figs. 1B and 3C). The effect of MACET proteins on microtubule polymerization rate was not consistent: some proteins increased the polymerization rate whereas others had the opposite effect (Fig. 2D).

Several values including frequency of stable microtubule ends and wavering microtubules, and polymerization and depolymerization rates were affected by the position of the GFP tag (Figs. 1B, C and 2C, D). Hence, the GFP tag may interfere with MACET activity. To test this possibility, we transiently expressed nontagged MACET4 under the control of a constitutive promoter from the vector that also expresses GFP in N. benthamiana plants stably transformed with a construct encoding a fusion between mCherry and Arabidopsis TuA5 (mCherry:TuA5) (Smertenko et al. 2020). We used the GFP-only vector as a negative control. N. benthamiana cells infiltrated with the construct showed cytoplasmic GFP signal (Supplementary Fig. S2 A). Tracking microtubule ends in cells expressing GFP revealed a higher frequency of stable ends (Supplementary Fig. S2, B and C). Analysis of the kymographs from microtubules demonstrated steeper depolymerization slopes in control cells expressing GFP than in cell expressing MACET4 (Supplementary Fig. S2 D). The rate of microtubule depolymerization was slower in cells expressing MACET4, whereas the polymerization rate was not affected (Supplementary Fig. S2 E). Thus, we can rule out that linking MACET proteins with GFP tag causes a drop in the tubulin OFF rate.

Analysis of microtubule ends and measuring microtubule dynamics resolved microtubule behavior on the scale of seconds (Figs. 1A, B and 2C, D). To determine the long-term stability of microtubules, we performed two experiments. First, we analyzed microtubule density as the number of microtubules per 10  $\mu$ m<sup>2</sup> and total microtubule length per  $\mu$ m<sup>2</sup> in N. benthamiana leaf pavement cells ectopically expressing GFP-MACET1, MACET1-GFP, GFP-MACET4, MACET4-GFP, GFP-MACET5, or MACET5-GFP. We scored at least three lobes from each of six cells for microtubule density, and total length of microtubules per µm<sup>2</sup> (Fig. 3A). Both MACET1 and MACET4 caused a higher total length of microtubules, whereas the total number of microtubules was not affected (Fig. 3, C and D). Ectopic expression of MACET5 fusions did not affect total microtubule length per µm<sup>2</sup> and caused a decrease in microtubule density only in the case of the GFP-MACET5 fusion.

In the second experiment, we treated infiltrated leaves with the microtubule polymerization inhibitor amiprophos methyl (APM). After APM treatment, microtubules should be more abundant in cells with slower microtubule depolymerization. We treated leaves expressing MACET fusion constructs with 20  $\mu$ M APM for 75 min, after which we imaged and scored them as above (Fig. 3, B, E, and F). The total microtubule length was greater in cells expressing MACET1 or MACET4 (Fig. 3E) and the total number of microtubules was greater in cells expressing MACET1, MACET4 or

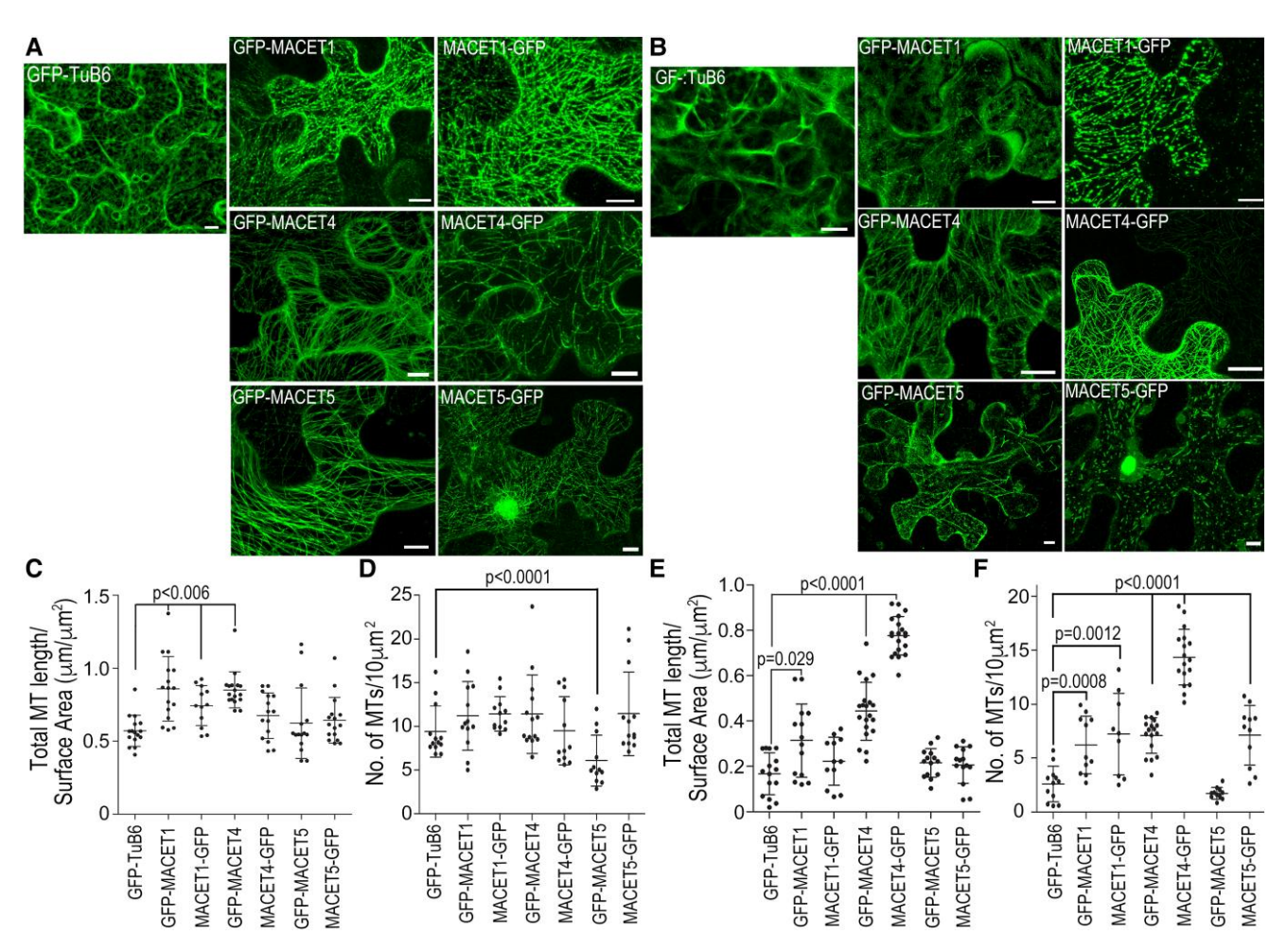


**Figure 3.** Long-term microtubule stability in *N. benthamiana* leaf pavement cells expressing *MACET1*, *MACET4*, or *MACET5*. **A)** Images of mocktreated (DMSO only) cells from *N. benthamiana* leaves infiltrated with the corresponding construct. Scale bars, 10 μm. **B)** Images of APM-treated leaves infiltrated with *GFP-TuB6* and the indicated *MACET-GFP* or *GFP-MACET* fusion construct. Scale bars, 10 μm. **C)** Total microtubule length per cell surface area (μm/μm²) in cells expressing *MACET1* or *MACET4* is higher relative to control cells expressing *GFP-TuB6*. **D)** The number of microtubules per 10 μm² of cell surface decreases only in cells expressing *GFP-MACET5*, whereas no significant changes were detected in cells expressing other fusion constructs. Each treatment was compared to the control using a two-tailed, unpaired t-test with no correction. *GFP-TuB6*, n = 6 cells; *GFP-MACET1*, n = 6 cells; *MACET1-GFP*, n = 4 cells; *GFP-MACET4*, n = 5 cells; *MACET4-GFP*, n = 4 cells; *GFP-MACET5*, n = 6 cells. **E)** Total cortical microtubule length per cell surface area (μm/μm²) after APM treatment. **F)** The number of microtubules per 10 μm² in APM-treated leaves is higher in cells expressing a *MACET* construct except for *GFP-MACET5* than in control cells expressing *GFP-TuB6*. Each treatment was compared to the control using a two-tailed, unpaired t-test with no correction for a non-Gaussian distribution. Scale bars, 10 μm. *GFP-TuB6*, n = 5 cells; *GFP-MACET1*, n = 5 cells; *MACET4-GFP*, n = 5 cells;

MACET5 compared to control cells expressing GFP-TuB6 (Fig. 3F). The total microtubule length and the microtubule density after APM treatment were lower in cells expressing MACET1-GFP, GFP-MACET1, MACET5-GFP, or GFP-MACET5 relative to the untreated control, but not in cells expressing MACET4-GFP (Fig. 3, C and E). This outcome shows that MACET4 suppresses microtubule depolymerization on the scale of hours.

#### Analysis of MACET gene expression

MACET paralogs are likely to function redundantly by decreasing the tubulin OFF rate if expressed in the same cell. To test this possibility, we analyzed the activity of MACET

promoters by cloning each promoter upstream of the reporter gene β-GLUCURONIDASE (GUS) in transgenic Arabidopsis lines. The MACET1 promoter is active in the xylem vessels of roots and cotyledons (Sasaki et al. 2017) and the MACET4 promoter is active in root and shoot apical meristems, young organs, and developing vascular bundles (Schmidt and Smertenko 2019). The promoters of MACET2, MACET3, and MACET6 were active in reproductive organs (Table 1; Supplementary Figs. S3 and S4). The MACET2 promoter was active in ovules and the vasculature of developing petals, the MACET3 promoter was active in ovules and pollen grains, the MACET6 promoter was active only in pollen grains and in pollen tubes

(Supplementary Fig. S3 A to E). The promoters of MACET5 and MACET7 were active in root and shoot apical meristems (Supplementary Fig. S4 A to G; Table 1). Furthermore, the MACET5 promoter was active in differentiating vascular bundles of roots, leaves, and flowers, all cells of expanding leaves, and developing styles (Supplementary Fig. S4, B and C). MACET7 promoter was active at the distal edges of developing petals and vasculature of young leaves (Supplementary Fig. S4, E and G). The promoters of MACET3, MACET4, MACET5, and MACET7 were also active in developing embryos (Supplementary Fig. S4 H).

We compared the localization of MACET5 and MACET7 in dividing root apical meristem to the published localization of MACET4 based on the *mce4-1 proMACET4:MACET4-GFP* line (Schmidt and Smertenko 2019). MACET5-GFP accumulated only in dividing cells of the meristem, and GFP signal was undetectable in the root elongation zone (Supplementary Fig. S4 I). It was not possible to verify the localization of MACET7-GFP because the fluorescence signal was below the sensitivity of our microscope or the protein was not produced.

We noticed that the intracellular localization of MACET4-GFP and MACET5-GFP differs throughout cell division. MACET4-GFP localized predominantly to the phragmoplast distal zone during cytokinesis and around the daughter nuclei (Fig. 4, A to C), whereas MACET5-GFP localized to the phragmoplast distal zone and inside nuclei (Fig. 4, D to F). Expression of GFP-MACET5 or MACET5-GFP in N. benthamiana leaf pavement cells also resulted in both nuclear localization and microtubule labeling (Supplementary Fig. S1 A).

#### Functions of MACETs in the phragmoplast

A macet4 knockout was shown to cause longer phragmoplasts (Schmidt and Smertenko 2019). Longer phragmoplasts were also reported in the case of a macet4 macet5 double mutant (Sasaki et al. 2019). These results suggest that MACET proteins regulate microtubule dynamics during cytokinesis. The overlapping expression patterns and apparent functional redundancy necessitate generation of higher-order mutants for determining the role of MACET in cytokinesis. Hence, we generated the mce4-1 mce5 double knockout by mutagenizing MACET5 using clustered regularly interspaced short palindromic repeat (CRISPR)/CRISPR-associated nuclease 9 (Cas9)-mediated gene editing in the macet4-1T-DNA mutant background (Supplementary Fig. S5 A). A deletion of adenine at 147 bp downstream from the ATG causes a frameshift that leads to a loss of identity with MACET5 as amino acid position 48 and a premature STOP codon at the amino acid position 151. The rosette, whole plants, and flowers of the mutant plants appeared morphologically normal (Supplementary Fig. S5, B to D). The root growth of Col-0 and mce4-1 mce5 seedlings was indistinguishable (Supplementary Fig. S5, E and F). Analysis of meristem length of seedlings grown on normal medium or on medium supplemented with propyzamide, an inhibitor of microtubule polymerization, showed no discernible differences between the apical meristem size in Col-0 and *mce4-1 mce5* under either growth condition (Supplementary Fig. S5 G).

To determine the role of MACET proteins in phragmoplast asymmetry, we attempted to measure microtubule dynamics in the phragmoplasts of *mce4-1 mce5* root meristem cells using fluorescence recovery after photobleaching (FRAP). However, transgenes encoding the common microtubule markers TuB6 or TuA5 fused to GFP or mCherry driven by the cauliflower mosaic virus (CaMV) 35S promoter were either silenced in the mutant background or exhibited low expression levels. In cells with acceptable fluorescence signal, higher zoom settings required for FRAP experiments caused photobleaching.

To overcome this technical challenge, we produced a new tubulin marker. We reasoned that a tubulin isotype upregulated in dividing cells would be more suitable for the analysis of microtubule dynamics in the phragmoplast than isotypes expressed in the differentiated tissues. Analysis of the publicly available Arabidopsis gene expression database (https://bar.utoronto.ca/efp2/) revealed higher abundance of  $\beta$ -tubulin2 (TuB2; At5g62690) transcripts in the root and shoot apical meristems, developing flowers, and embryos relative to differentiated organs. To overcome the photostability problem, we used the mNeonGreen fluorescent protein (Shaner et al. 2013) to produce the proTuB2:mNeonGreen-TuB2 construct.

We generated a homozygous transgenic line in Arabidopsis Col-0 using the proTuB2:mNeonGreen-TuB2 construct. The plants were morphologically normal and showed no signs of organ twisting or skewing (Supplementary Fig. S6, A to C) as was reported for the tubulin marker TuA6 (Abe and Hashimoto 2005). The root growth rate was similar to that of the GFP-TuB6 line used as a negative control (Supplementary Fig. S6, D and E). mNeonGreen-TuB2 signal was strong in the root meristem and transition zones, but not in the root differentiation zone or columella cells under the same image acquisition settings (Supplementary Fig. S7, A to C). We also detected higher fluorescence intensity in young leaves and the shoot apical meristem relative to differentiated leaves, petals, and hypocotyl (Supplementary Fig. S7, D to H). We succeeded in detecting the fluorescence signal in differentiated tissues at higher laser power and digital gain settings. All four major microtubule arrays (cortical microtubules, preprophase band, spindle and the phragmoplast) were labeled by the construct Arabidopsis root apical meristem cells (Supplementary Fig. S7, I to K) and in tobacco BY-2 tissue culture cells (Supplementary Fig. S7, L to O).

We measured the microtubule dynamics in the phragmoplasts of BY-2 cells expressing *mNeonGreen-TuB2* by FRAP. These experiments demonstrated that the mNeonGreen signal recovers faster in the midzone than in the distal zone (Supplementary Fig. S7, P to R). Similar results have been reported for different tubulin markers (Smertenko et al. 2011; Murata et al. 2013). High expression levels of *mNeonGreen-TuB2* in the root apical meristem cells together with higher quantum yield and photostability of

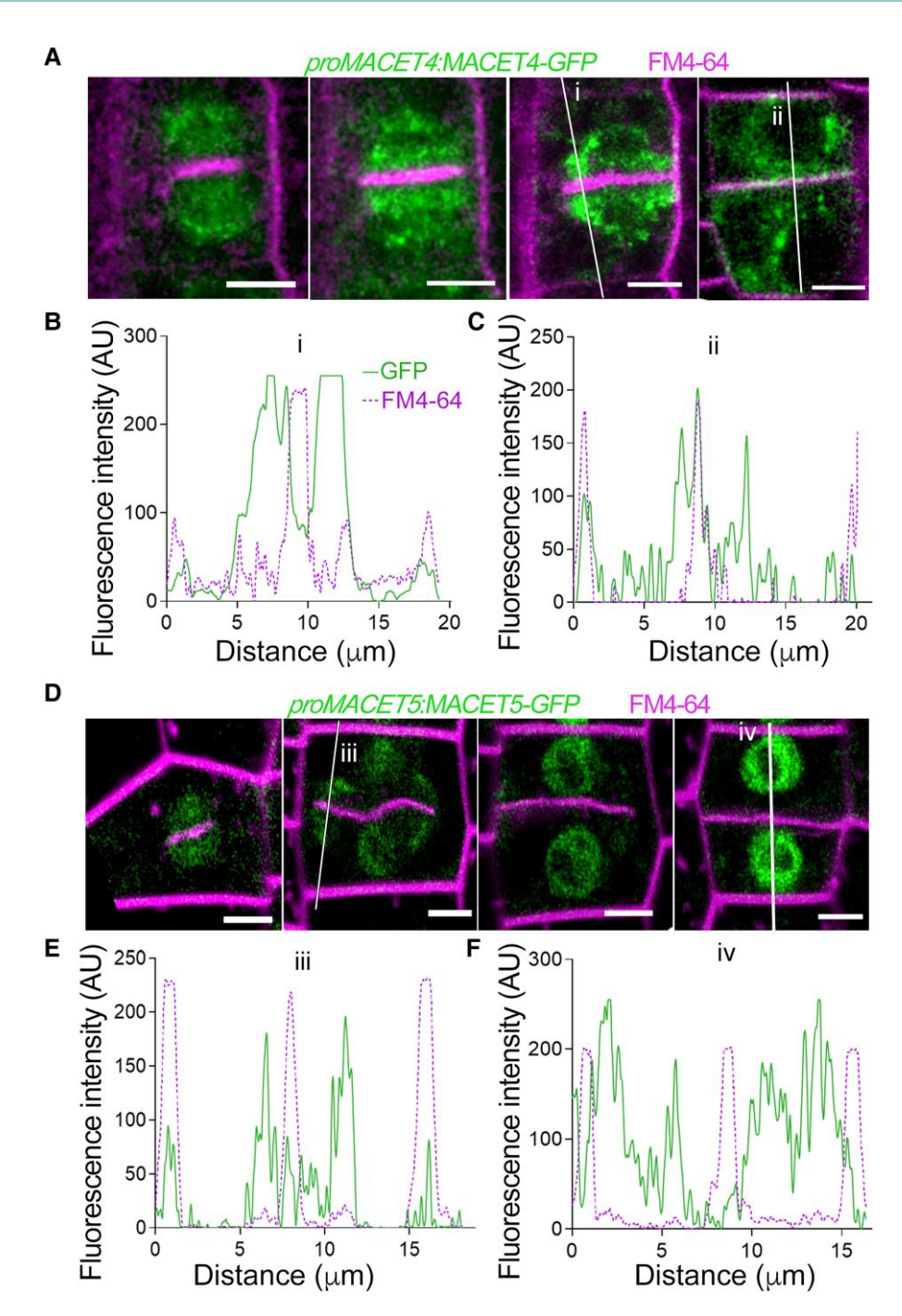


**Figure 4.** Intracellular localization of MACET4-GFP and MACET5-GFP in dividing Arabidopsis cells. **A)** Representative images of Arabidopsis root cells harboring *proMACET4:MACET4-GFP* during successive stages of cytokinesis. Cell membranes stained with 2  $\mu$ M FM464 are shown in magenta. Lines labeled with Roman numerals i and ii represent phragmoplast leading edge and postcytokinesis MACET4 localization used for plot intensity profiles, respectively. Scale bars, 5  $\mu$ m. **B)** GFP fluorescence plot intensity profile taken through the phragmoplast (line i). **C)** GFP fluorescence plot intensity profile taken through postcytokinetic cell (line ii). **D)** Representative images of Arabidopsis root cells harboring *proMACET5:MACET5-GFP* during successive stages of cytokinesis. Cell membranes stained with 2  $\mu$ M FM464 are shown in magenta. Lines labeled with Roman numerals iii and iv represent phragmoplast leading edge and post cytokinesis MACET5 localization used for plot intensity profiles, respectively. Scale bars, 5  $\mu$ m. **E)** GFP fluorescence plot intensity profile taken through the phragmoplast (line iii). **F)** GFP fluorescence plot intensity profile taken through post-cytokinetic cell (line iv).

mNeonGreen permitted imaging cells at lower laser power (0.25%) for the 1 to 2 min of the FRAP experiment without discernible photobleaching.

To determine the role of MACET4 in phragmoplast microtubule dynamics, we introduced the *proTuB2*: *mNeonGreen-TuB2* construct into the *mce4-1* mce5 mutant

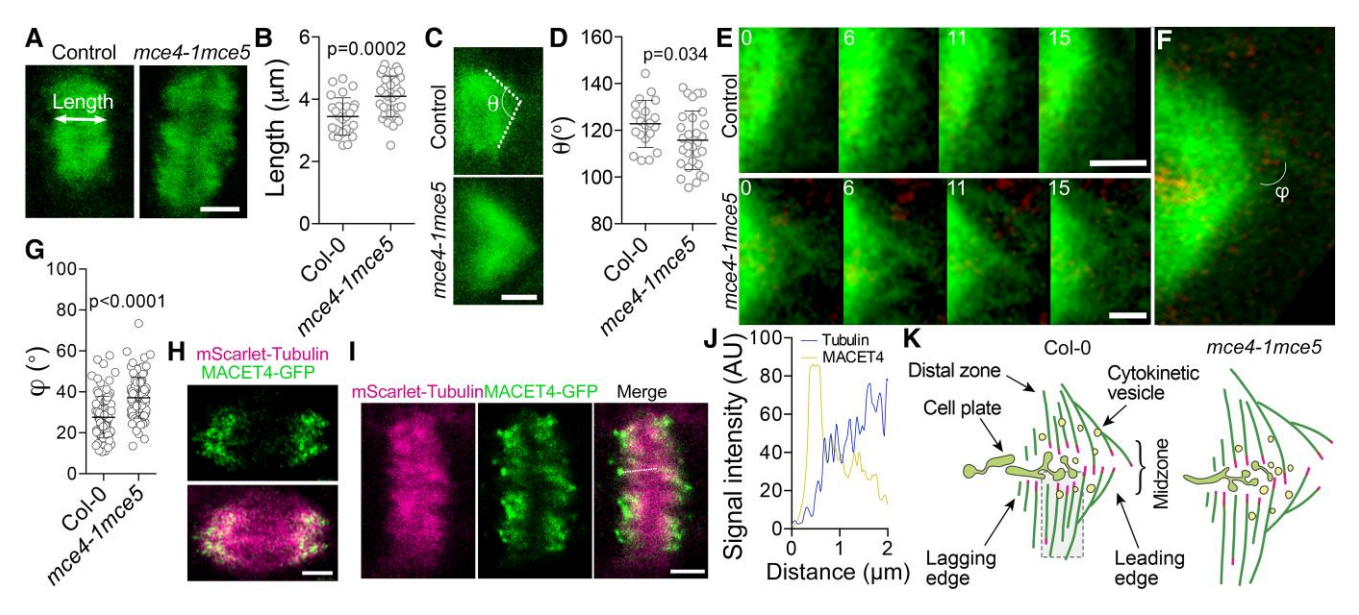
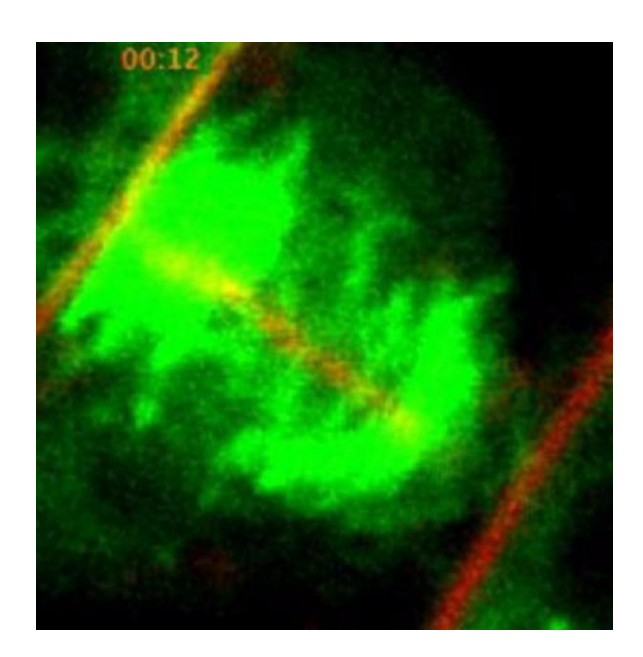


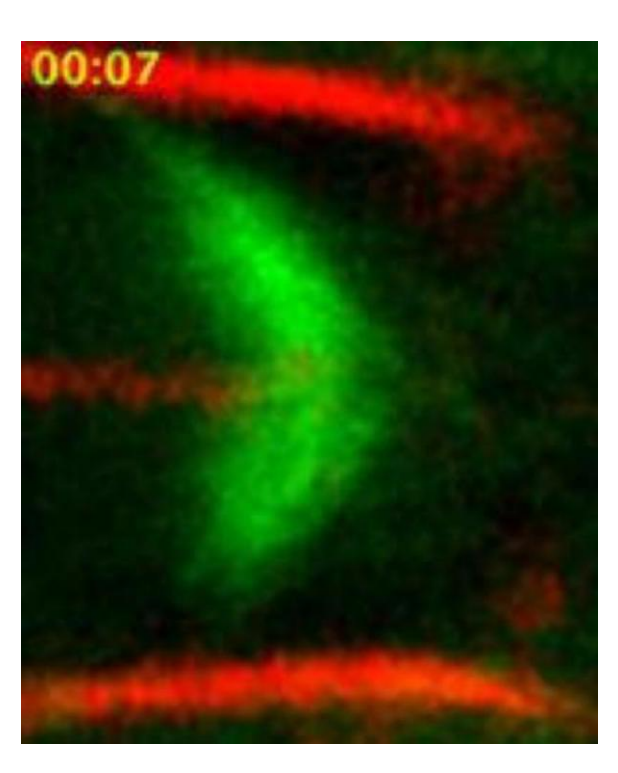
Figure 5. Microtubule nucleation is abnormal in mce4-1 mce5 phragmoplasts. A and B) mNeonGreen-TuB2 labeling of phragmoplast (A) and phragmoplast length (B) in root apical meristem cells of Col-0 and mce4-1 mce5. Scale bar, 2.5  $\mu$ m. The P-value was determined by a t-test with no correction (n=27 for Col-0 and n=33 for mce4-1 mce5 phragmoplasts measured in 10 different roots). C and D) Representative images of the phragmoplast leading edge in Col-0 and mce4-1 mce5 (C) labeled by mNeonGreen-TuB2, and the leading edge angle D (D). Scale bar, 2  $\mu$ m. The P-value was determined by a t-test with no correction (n=20 for Col-0 and n=30 for mce4-1 mce5 phragmoplasts measured in 10 different roots). E) Representative images of microtubule nucleation events at the phragmoplast leading edge in Col-0 and mce4-1 mce5 cells expressing mNeonGreen-TuB2. Scale bars, 1  $\mu$ m. F and G) Angle of microtubule nucleation at the phragmoplast leading edge ( $\phi$ ) of Col-0 and mce4-1 mce5 root apical meristem cells harboring proTuB2:mNeonGreen-TuB2. The membranes were stained with FM4-64. The P-value was calculated using a t-test (n=87 for Col-0 and n=103 for mce4-1 mce5 individual nucleation events measured in different 10 phragmoplasts). H and I) Localization of MACET4-GFP in the anaphase spindle (H) and the phragmoplast (I) in cells expressing mScarlet-TuB2. Scale bars, 2  $\mu$ m. J) Fluorescent signal intensity measured along the line in panel I. K) Diagram explaining the mce4-1 mce5 phenotype. Microtubules are green filaments with their plus ends highlighted in magenta. The shape of the phragmoplast leading edge depends on the angle of branched microtubule nucleation. In the mutant, greater angle of microtubule nucleation generates a sharper leading edge and microtubules are longer. The gray rectangle shows the part of the phragmoplast that was used for the modeling experiments.

by transformation. The phragmoplasts in the root apical meristem cells of mce4-1 mce5 were longer and the phragmoplast leading edge was sharper relative to Col-0 (Fig. 5, A to D). It was possible to resolve branched nucleation events at the leading edge (Fig. 5E). Microtubules from the opposite halves of the phragmoplast met at the midzone, interacted with each other, and became incorporated into the phragmoplast main body in both control and mce4-1 mce5 (Fig. 5E; Video 3 and 4). We measured the angle of branched nucleation  $\phi$  relative to the phragmoplast body (Fig. 5F) and determined that mce4-1 mce5 shows an increase in  $\phi$  from 25° to 40° (Fig. 5G).

We also generated transgenic Arabidopsis lines with the *proTuB2:mScarlet-TuB2* construct. These transgenic plants lacked a discernible phenotype and the construct labeled all mitotic microtubule arrays (Supplementary Fig. S7, T to X), although the signal intensity and photostability were comparable to the published mCherry–TuB6 reporter. For the latter reasons, it was not feasible to perform FRAP experiments with this marker. We thus introduced *proTuB2: mScarlet-TuB2* in the *mce4-1 proMACET4:MACET4-GFP* background by crossing. MACET4-GFP localized to puncta in the



**Video 3.** Microtubule dynamics in the phragmoplast leading zone of a Col-0 root apical meristem cell harboring *proTuB2:mNeonGreen-TuB2*. Membranes were stained with FM4- 64.



**Video 4.** Microtubule dynamics in the phragmoplast leading zone of a *mce4-1 mce5* mutant root apical meristem cells harboring *proTuB2*: *mNeonGreen-TuB2*. Membranes were stained with FM4-64.

anaphase spindle poles (Fig. 5H) and the phragmoplast distal zones (Fig. 5I). All MACET puncta in the phragmoplast colocalized with the sites of microtubule nucleation and there was an apparent signal along the distal regions of microtubules (Fig. 5J). These data indicate that MACET4 contributes to microtubule nucleation at the distal zone and modulates the geometry of branched microtubule nucleation (Fig. 5K).

We compared microtubule turnover by FRAP in the phragmoplasts of Col-0 and mce4-1 mce5. In the control Col-0 cells, the recovery of fluorescent signal in the midzone was faster than in the distal zone (Fig. 6, A and B), whereas the recovery in the midzone and the distal zone was similar in mce4-1 mce5 (Fig. 6, A and C). Consistent with this outcome, the microtubule turnover rates  $(t_{1/2})$  in the distal zone and in the midzone were different in Col-0 but not in mce4-1mce5 (Fig. 6D). The average ratio between microtubule turnover in the distal zone and the midzone was significantly lower in the mutant than in control (1.07 versus 1.20; Fig. 6E). Thus, mce4-1 mce5 lacks axial asymmetry.

Comparison of kymographs revealed incomplete recovery of fluorescent signal in *mce4-1 mce5*, whereas the signal returned to almost pre-bleach levels in Col-0 (Fig. 6F). To determine the reason for this difference, we measured the immobile fraction of fluorescent signal in the above FRAP experiments, which represents a fraction of less dynamic microtubules. The immobile fraction in *mce4-1 mce5* was 60% higher than in the control (Fig. 6G). Therefore, phragmoplasts in *mce4-1 mce5* have a higher abundance of less dynamic microtubules.

### MACET4 interacts with y-tubulin and AUG7

The localization of MACET4-GFP at all microtubule nucleation sites in vivo (Schmidt and Smertenko 2019) and at microtubule nucleation sites in the phragmoplast (Fig. 51) suggested that MACET4 might cooperate with other microtubule-nucleating factors. To test this hypothesis, we identified MACET4-interacting proteins using three complementary approaches (Fig. 7A). The first was affinity chromatography using MACET4 as bait. In this experiment three columns served as negative controls. First, recombinant purified Arabidopsis Microtubule-Associated Protein 65-1 (MAP65-1) was selected for its predominant localization in the phragmoplast midzone (Smertenko et al. 2004). As MACET4 localizes predominantly to the distal zone, MACET4 and MAP65-1 are expected to have different interactomes. The second negative control was recombinant MAP20 from purple false brome (Brachypodium distachyon). MACET4 and BdMAP20 have high isoelectric points (pl 10.4 and pl 9.9, respectively), but BdMAP20 is expressed in differentiating cells of vascular bundles (Smertenko et al. 2020). Proteins interacting with both BdMAP20 and MACET4 would be most likely due to electrostatic interactions. Finally, as all recombinant proteins were produced in bacteria and therefore may have contaminating bacterial proteins, total protein extract from E. coli Rosetta II cells was a third negative control.

Considering that MACET4 is only present in dividing cells, we prepared protein extract from cell cycle-synchronized tobacco BY-2 cell cultures containing at least 40% of cells in telophase. Considering that frequency of dividing cells in Arabidopsis roots under our experimental conditions is 0.01% and dividing BY-2 cells are about 2.5 times bigger than dividing Arabidopsis root cells, we estimated that the abundance of MACET4 interactors in such extracts is about 10,000-fold higher than in extracts from Arabidopsis root tips. Proteins identified in all three negative controls were disregarded. Amongst the remaining proteins, we selected those whose encoding genes are expressed in the shoot or root apical meristems according to the EFP browser, culminating in the identification of four potential interactors: RabA4a, MITOTIC ARREST-DEFICIENT 2 (MAD2), CLIP-ASSOCIATED PROTEIN (CLASP), and AUG7 (Fig. 7B).

The second approach for identifying MACET4 interactors took into account the abundance of intrinsically disordered regions in its predicted secondary structure (Sasaki et al. 2019; Schmidt and Smertenko 2019). As disordered regions confer flexibility to the protein secondary structure, we reasoned that MACET4 conformation might change upon binding to microtubules resulting in a new interface with a different interactome (Fig. 7A). To test this hypothesis, we bound recombinant MACET4 to microtubules and pulled down interacting proteins from total protein extract prepared from the batch of telophase-enriched tobacco BY-2 cell cultures used above. The following negative controls were used: microtubule bundles formed with recombinant Arabidopsis MAP65-1, microtubules alone, and the three

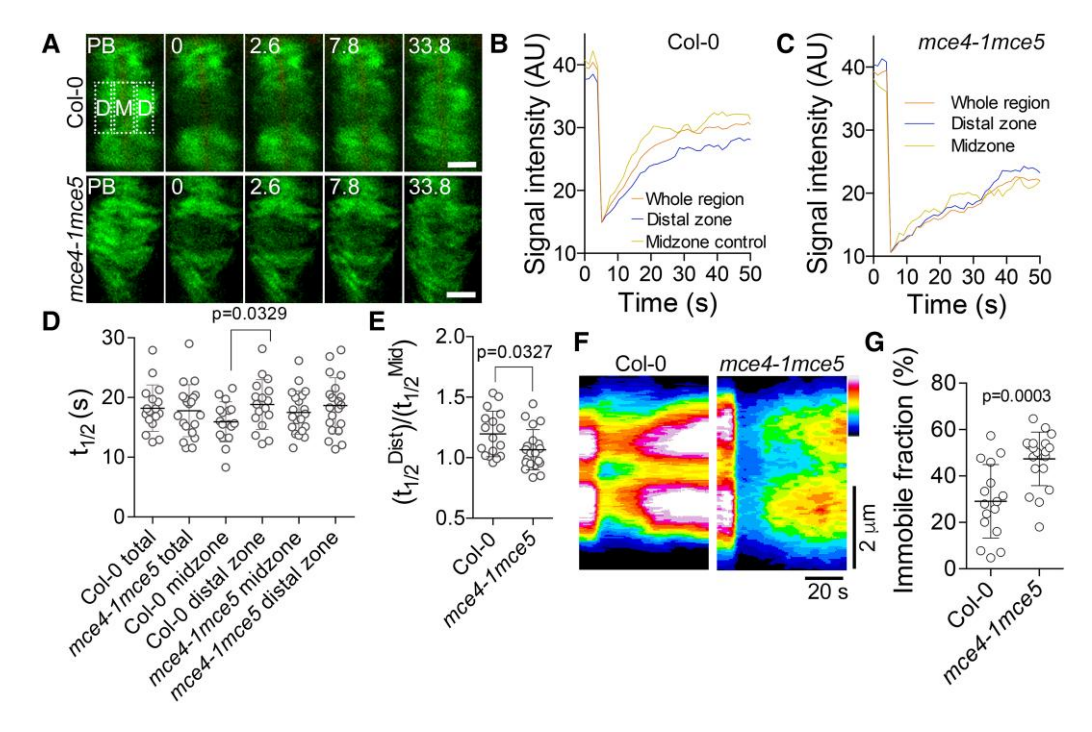


Figure 6. Phragmoplast axial asymmetry is lost in mce4-1 mce5. A) Representative frames from the phragmoplast FRAP time-lapse images in Col-0 and mce4-1 mce5 cells expressing mNeonGreen-TuB2. Numbers represent time in seconds. The first time point after bleaching is 0. PB, pre-breach frame. The rectangles indicate the regions of interests where the signal recovery was measured: D, distal zone; M midzone. Scale bars, 2 µm. B and C) Representative charts of fluorescence signal recovery in the distal zone, midzone, and combined midzone and distal zones (whole region) of Col-0 (B) and mce4-1 mce5 (C) cells expressing mNeonGreen-TuB2. The signal was normalized by the lowest values after bleaching. D) Microtubule turnover rate  $(t_{1/2})$  in the total bleached region, midzone, and distal zone of the phragmoplast in Col-0 and mce4-1 mce5 cells. The bleached regions are shown in **A**. The *P*-value was determined by a *t*-test with no correction (n = 17 for Col-0 and n = 20 for mce4-1 mce5 phragmoplasts measured in 12 roots). **E**) Ratio of  $t_{1/2}$  in the distal zone to the midzone in phragmoplasts of Col-0 and mce4-1 mce5 cells. The P-value was determined by a t-test with no correction (n = 17 for Col-0 and n = 20 for mce4-1 mce5 phragmoplasts measured in 12 roots). F) Representative kymographs of the phragmoplast FRAP experiment in Col-0 and mce4-1 mce5 root apical meristem cells. Horizontal scale bar, 20 s; vertical scale bar, 2 µm. G) Immobile fraction of the total fluorescent signal in phragmoplasts of Col-0 and mce4-1 mce5 cells. The P-value was determined by t-test with no correction (n = 17 for Col-0 and n = 20 for mce4-1 mce5 phragmoplasts measured in 12 roots).

negative controls used for the affinity chromatography experiment above. After proteins from all negative controls were disregarded, two unique MACET4 interactors whose encoding genes are expressed in the root and shoot apical meristems remained: CLASP and γ-tubulin (TUBG1).

Microtubule nucleation in phragmoplast asymmetry

The third approach was based on the observation that in addition to decorating microtubules, MACET4 localizes to puncta in vivo and forms "cores" with tubulin in vitro that can nucleate microtubules (Schmidt and Smertenko 2019). Plausibly, MACET4 plays a unique role in the cores and interacts with different proteins. To test this hypothesis, we produced cores by incubating recombinant MACET4 with a low concentration of tubulin (5  $\mu$ M). The protein extract was prepared from the same batch of tobacco BY-2 cells used for the above purifications and the same negative controls were used. After proteins in the negative controls were disregarded, we identified CLASP and γ-tubulin as potential interactors (Fig. 7B; Supplementary Table S1). This outcome demonstrates that the MACET4 interactomes in the microtubule-bound state and in the cores are similar.

We verified these interactions using bimolecular fluorescence complementation (BiFC) assays in N. benthamiana

leaf pavement cells. Accordingly, we cloned the AUG7 and TUBG1 coding sequences into the Gateway binary vectors pSITE-nEYFP or pSITE-cEYFP. Reconstitution of enhanced yellow fluorescent protein (EYFP) fluorescence occurred in cells expressing nEYFP-AUG7 (encoding the N-terminal half of the EYFP fused to AUG7) and MACET4-cEYFP (encoding MACET4 fused to the C-terminal half of EYFP) but not AUG7-cEYFP and MACET4-nEYFP. For BiFC assays with y-tubulin, EYFP reconstitution occurred in cells expressing nEYFP-TUBG1 and MACET4-cEYFP as well as in cells with TUBG1-cEYFP and MACET4-nEYFP. The combination of nEYFP-AUG7 and nEYFP-TUBG1 was used as a positive control and the combination of nEYFP-ROP6 and MACET4-cEYFP was used as a negative control (Supplementary Fig. S8 A). Combination of empty vectors did not produce a detectable signal. Co-expression of AUG7-GFP with MACET4-mCherry resulted in decoration of microtubules by AUG7-GFP, whereas, AUG7-GFP was cytoplasmic in the absence of MACET4mCherry (Supplementary Fig. S8, B and C).

We validated the interaction between MACET4 and AUG7 using co-sedimentation assays. Recombinant AUG7 did not co-sediment with taxol-stabilized microtubules (Fig. 7C)

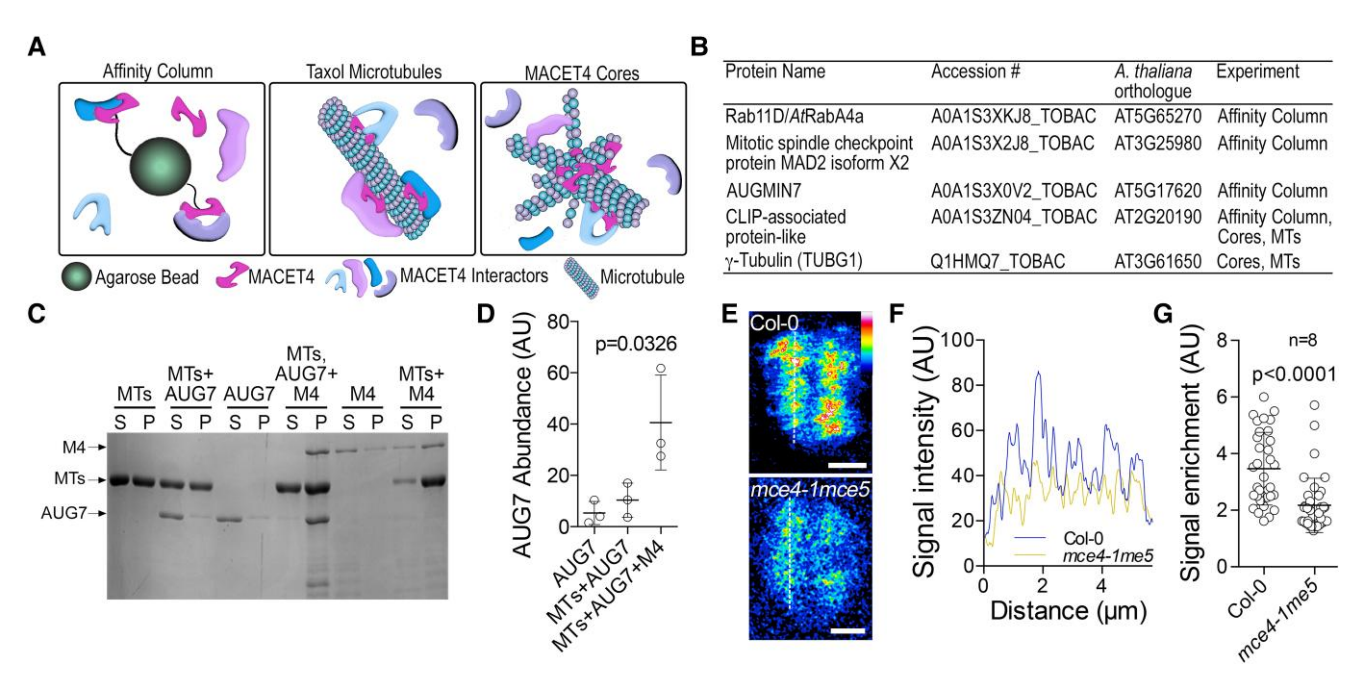


**Figure 7.** MACET4 interacts with γ-tubulin and AUGMIN7. **A)** Diagram illustrating the three approaches employed to identify MACET4 interactors: affinity chromatography, microtubule pull down, and cores pull down. Association of MACET4 with microtubules or cores can create new interfaces with a unique set of interacting partners. **B)** List of identified MACET4 interacting proteins. **C)** A representative SDS-PAGE gel showing cosedimentation assay of MACET4 and AUG7 with taxol-stabilized microtubules. Protein composition in each reaction is indicated above the gel. M4, MACET4; MTs, microtubules; S, supernatant; P, pellet. **D)** Quantification of the AUG7 band intensity in the pellet on the gel shown in C. The amount of AUG7 that binds to microtubules in the presence of MACET4 is significantly higher than in the controls. The P-value of unpaired *t*-test shows significance of difference between AUG7 band intensity in MTs + AUG7 and MTs + AUG7 + M4 (n = 3, independent co-sedimentation assays). **E)** Localization of AUG7-mNeonGreen in the phragmoplast of Col-0 and *mce4-1 mce5*. Scale bars, 2 μm. **F)** Intensity of AUG7-mNeonGreen fluorescence measured along white broken lines in E. The intensity of peaks is greater in the Col-0 than in *mce4-1 mce5*. **G)** Enrichment of AUG7-mNeonGreen signal in puncta relative to the background in the phragmoplasts of Col-0 and *mce4-1 mce5*. The P-value was calculated using an unpaired *t*-test (8 cells per each line, 33 puncta analyzed). The P-value was determined by a *t*-test with no correction (n = 33 for Col-0 and n = 38 for *mce4-1 mce5* phragmoplasts measured in 25 roots).

and the amount of AUG7 in the pellet was the same as in the control reaction without microtubules (Fig. 7D). However, in the presence of MACET4, AUG7 was present in the pellet with microtubules (Fig. 7, C and D). Thus, MACET4 tethers AUG7 to microtubules in vitro. Next, we examined the effect of AUG7 on MACET4 activity using a turbidimetric assay. Turbidity of a tubulin solution in the presence of recombinant MACET4 increased relative to that of tubulin only (Supplementary Fig. S8 D). Adding AUG7 to the polymerization mixtures with MACET4 did not amplify the effect of MACET4 on the turbidity values. Consistent with this outcome, the increase of bulk tubulin polymer abundance caused by 2  $\mu$ M MACET4 was not affected by AUG7 (Supplementary Fig. S8, E and F). Thus, AUG7 and MACET4 do not cooperate in microtubule polymerization.

If MACET4 functions as an AUG7 tethering factor, then the localization of AUG7 should be affected in *mce4-1 mce5*. To test this idea, we introduced a *proAUG7:AUG7-mNeonGreen* transgene into *mce4-1 mce5* and compared the localization of AUG7-mNeonGreen in the phragmoplast of *mce4-1 mce5* and Col-0. In control cells, AUG7 formed puncta of bright fluorescence along phragmoplast microtubules (Fig. 7E). The intensity of these puncta was lower in the

phragmoplasts of *mce4-1 mce5* (Fig. 7, E and F). We measured the ratio of mNeonGreen signal in the puncta to the signal intensity near the puncta and found significantly lower values in the double mutant (Fig. 7G).

Next, we examined whether AUG7 plays a role in the localization of MACET4 using the published aug7-1 allele (Hotta et al. 2012). We introduced the proMACET4:MACET4-GFP transgene into aug7-1 through crossing. As homozygous aug7-1 plants are sterile, all experiments were performed on plants with the aug7-1 phenotype isolated from the segregating progeny of a heterozygous parent (Fig. 8A). Localization and enrichment of MACET4 was not affected in aug7-1 (Fig. 8, B and C). To analyze phragmoplast morphology and microtubule dynamics in aug7-1, we introduced the proTuB2:mNeonGreen-TuB2 transgene into aug7-1 through crossing. We determined that the phragmoplasts in aug7-1 are longer than in the Col-0 control (Fig. 8, D and E) but the leading edge angle and the angle of branched microtubule nucleation in aug7-1 were not affected (Fig. 8, F and G). Microtubule turnover  $(t_{1/2})$  and the axial asymmetry were also not affected in aug7-1 (Fig. 8, H and J) but the immobile fraction was greater in aug7-1 than in Col-0 (Fig. 81) and the phragmoplast expansion rate was slower

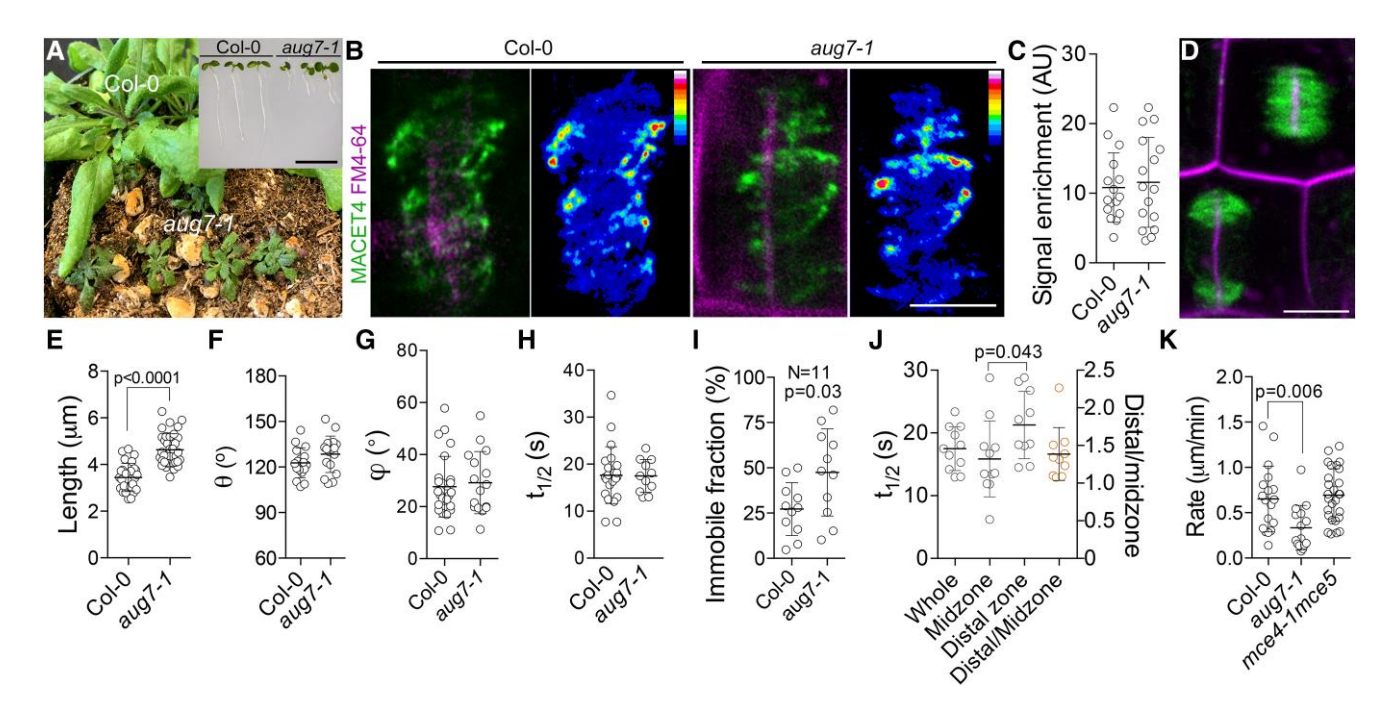


**Figure 8.** Analysis of the *aug7-1* mutant. **A)** Representative images of 6-wk-old Col-0 and *aug7-1* plants. Inset shows 1-wk-old seedlings. Scale bar, 10 mm. **B)** Representative images of MACET4-GFP localization in phragmoplast of Col-0 and *aug7-1*. Scale bar, 5 μm. The membranes were stained with FM4-64. **C)** Signal enrichment at the MACET4-GFP puncta in Col-0 and *aug7-1* (n = 16 Col-0 and 16 *aug7-1* phragmoplasts in 10 roots). **D)** Phragmoplasts in *aug7-1* expressing *mNeonGreen-TuB2*. Scale bar, 5 μm. The membranes were stained with FM4-64. **E)** Phragmoplast length in Col-0 and *aug7-1*. The *P*-value was determined by a t-test with no correction (n = 33 for Col-0 and n = 38 for *mce4-1 mce5* phragmoplasts in 25 roots). **F)** Phragmoplast leading edge angle (θ) in Col-0 and *aug7-1* root apical meristem cells. The membranes were stained with FM4-64. The *P*-value was calculated using a *t*-test (n = 17 for Col-0 and n = 17 for *mce4-1 mce5* phragmoplasts in 9 roots). **G)** Angle of microtubule nucleation at the phragmoplast leading edge (φ) of Col-0 and *aug7-1* root apical meristem cells. The membranes were stained with FM4-64. The *P*-value was calculated using a *t*-test (n = 26 for Col-0 and n = 16 for *mce4-1 mce5* individual nucleation events measured in 10 phragmoplasts). **H and I)** Phragmoplast microtubule turnover rate ( $t_{1/2}$ ) (H) and immobile fraction of GFP signal in Col-0 and *aug7-1* phragmoplast (I). The *P*-value was calculated using a *t*-test (n = 22 for Col-0 and n = 11 for *mce4-1 mce5* phragmoplasts measured in 9 roots). **J)** Microtubule turnover rate ( $t_{1/2}$ ) in the phragmoplast total bleached region, midzone, and distal zone, and ratio of ( $t_{1/2}$ ) values in the distal zone and the midzone of *aug7-1*. The location of bleached regions is shown in Fig. 6A. The *P*-value was determined by a *t*-test with no correction (n = 10 phragmoplasts measured in 8 roots). **K)** Phragmoplast expansion rate in Col-0, *aug7-1*, and *mce4-1 mce5*. The *P*-value was cal

in *aug7-1* than in Col-0 or *mace4-1 mce5* (Fig. 8K). Therefore, MACET4 functions as an AUG7 tethering factor, and MACET4 and AUG7 play overlapping but different roles in the phragmoplast.

To check the genetic interaction between MACET and AUG7, we crossed aug7-1 (as female parent) to macet4-1 macet5 (as the male parent). The F1 population appeared morphologically normal. Genotyping the F2 population for homozygous macet4-1 macet5 yielded 17 individuals out of 126 (13.5%). Out of these 17 plants, none were homozygous for aug7-1 and 7 plants were heterozygous. Hence, the triple macet4-1 macet5 aug7-1 knockout mutant is not viable.

## Microtubule nucleation determines phragmoplast asymmetry

The microtubule turnover rate  $(t_{1/2})$  in FRAP experiments depends on how fast new microtubules populate the bleached area, which is determined by microtubule nucleation and growth rates. Considering that MACET4 and

MACET5 localize to the microtubule nucleation sites and function in decreasing the tubulin OFF rate, we hypothesized that partial loss of phragmoplast asymmetry in mce4-1 mce5 might be caused by defects in microtubule nucleation. As imaging individual microtubules in the phragmoplast of living cells remains out of reach even using higher resolution microscopy (Vyplelová et al. 2018), we used modeling to test this hypothesis. Our model simulated FRAP experiments in one half of the phragmoplast corresponding to the transition zone where microtubule nucleation and depolymerization are balanced (gray rectangle in Fig. 5K). The model was based on published values of microtubule dynamics (Shaw et al. 2003) and the following rules: (1) there is a finite amount of tubulin in a cell; (2) the rates of microtubule polymerization, transition from pause to growth, transition from catastrophe to pause, transition from catastrophe to growth are proportional to the available tubulin concentration, whereas rates of catastrophe, transition from growth to pause or catastrophe rate are inversely proportional to the free tubulin concentration; (3) the position of microtubule

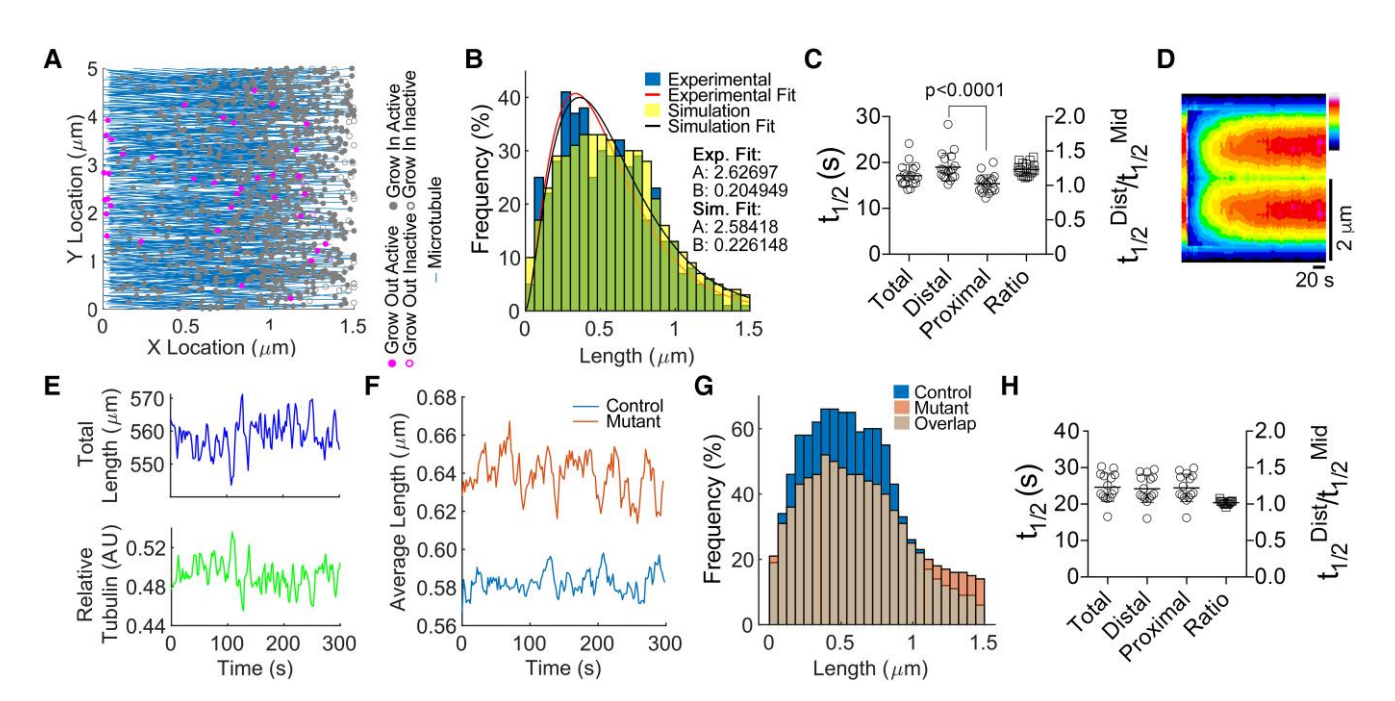


**Figure 9.** Microtubule nucleation maintains phragmoplast asymmetry and size. **A)** A representative image of a simulation experiment in which microtubules originate from nucleation sites (seeds) and can grow towards the midzone located at the x = 0 (Grow In) or toward the distal zone located at x = 1.5 (Grow Out). The reseeding rate determines the number of active nucleation sites. **B)** Distribution of microtubule length in electron micrographs and in the simulations. Exponential fit demonstrated a close match of distributions with A = 2.62697, B = 0.204949 for the experimental data and A = 2.58418, B = 0.226148 for the simulation data. **C)**  $t_{1/2}$  in the total bleached region, midzone and distal zone (left y-axis); and ratio of  $t_{1/2}$  in the distal zone to the midzone (right y-axis) in the simulated FRAP experiments. Statistical significance of differences between the datasets was determined using a parametric t-test (n = 19 independent simulations). **D)** A representative kymograph of simulated FRAP experiment. Horizontal scale bar, 20 s; vertical scale bar, 2  $\mu$ m. **E)** Free tubulin content and total microtubule length values over the duration of a representative simulation. **F)** Average microtubule length over the duration of whole simulations representing control and mce4-1 mce5 phragmoplast. The mutant was simulated by decreasing the microtubule re-seed rate (r\_reseed rate). **G)** Distribution of microtubule length in simulations representing control and mce4-1 mce5 phragmoplast (15 independent simulations were performed). **H)**  $t_{1/2}$  in the total bleached region, midzone and distal zone (left y-axis); and ratio of  $t_{1/2}$  in the distal zone to the midzone (right y-axis) in the simulated FRAP experiments of mce4-1 mce5 phragmoplast.

nucleation sites and polarity of microtubules nucleated at each side are fixed, but the site can be either in an active or an inactive state (Fig. 9A; Supplementary Fig. S9, A to C); and (4) the phragmoplast length is 1.5  $\mu$ m, in line with the size of Arabidopsis phragmoplasts.

Parameters of the model were fitted to approximate three types of experimental data (Fig. 9, B to D). The first type was the distribution of microtubule length, determined from the electron tomography data generated by the laboratory of Andrew Staehelin (Fig. 6A in Austin et al. 2005). The second type was experimental values of microtubule turnover rates and the asymmetry between the distal and proximal zones. The third type was kymographs of the mNeonGreen-TuB2 in FRAP experiments. The resulting parameters are listed in Supplementary Table S2. However, these parameters were subject to the above Rule 2. Variability of the microtubule turnover rates generated in 19 independent simulations in our model (Fig. 9C) showed consistency with the stochastic nature of microtubule dynamics in living cells (Fig. 6D). We observed that the kymograph data generated by the simulation resembles that of the living cells (Figs. 7F and 9D). Further validation included examining the relationships between tubulin monomers and oligomers during the simulations. The total microtubule polymer length values generated spikes throughout the time course of the simulation (Fig. 9E); each spike was accompanied by the decrease in free tubulin concentration. Thus, our model accurately represents the relationships between microtubule polymerization and free tubulin.

To simulate the *mce4-1 mce5* knockout, we lowered the microtubule nucleation rate using the parameter "r\_reseed" that determines how soon a nucleation site (seed) generates a new microtubule after the previous microtubule depolymerizes. In the control situation, this parameter was set to 1, and in the mutant simulations this parameter was decreased to 0.5. This change caused fewer active nucleation sites in each time frame by an average of 15.4% (975.8 versus 825.2; Supplementary Fig. S9 D). All other parameters remained the same. A decrease in microtubule nucleation caused a greater amount of free tubulin and lower total microtubule polymer relative to the control, as expected (Supplementary Fig. S9, E and F). While the total microtubule

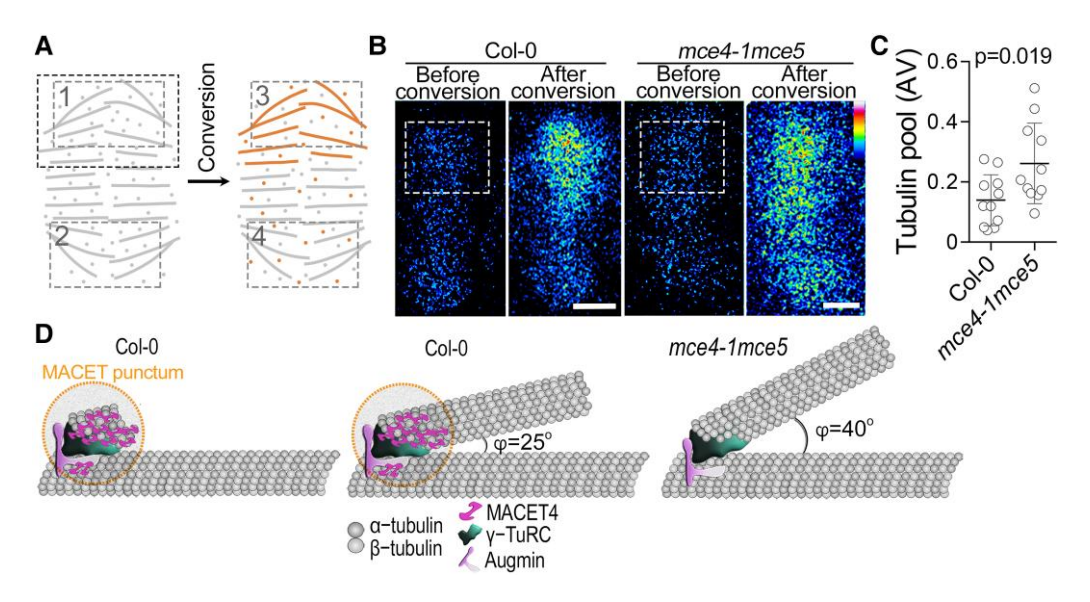
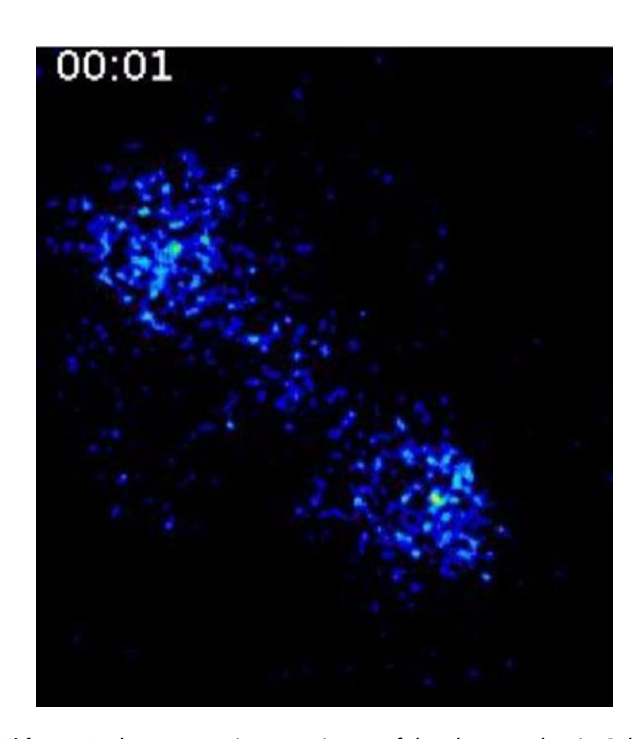


**Figure 10.** Quantification of relative tubulin abundance during cytokinesis in Arabidopsis. **A)** The principle for quantification of tubulin abundance. Tubulin exists in two states: as a microtubule polymer and in a free pool. Photo-conversion of EosFP-TuB2 in region of interest 1 will activate red fluorescence for both states. Microtubules will remain within region 3 and free tubulin will diffuse through the cytoplasm resulting in a fluorescent signal in region of interest 4. It is possible to quantify the relative tubulin pool using fluorescence values in all four regions of interest. **B)** Representative images of phragmoplasts from Col-0 and *mce4-1 mce5* before and after photo-conversion of EosFP. Rectangles show the photo-converted areas. Scale bars, 2 μm. **C)** Relative tubulin pool abundance in Col-0 and *mce4-1 mce5*. Statistical significance was calculated using a *t*-test (n = 11 phragmoplasts were analyzed for each mutant in 8 different roots). **D)** Three roles of MACET4 in microtubule nucleation: lowering the tubulin OFF rate within a punctum proximally to γ-TuRC; altering the angle of branched microtubule nucleation; tethering AUG7 to microtubules. Once the microtubule grows outside the punctum, the effect of MACET ceases and other proteins govern microtubule fate. Knockout of *MACET4* and *MACET5* causes greater branched nucleation angle.

polymer was lower in the mutant relative to the control throughout the simulation, the average microtubule length was greater in the mutant (Fig. 9F) due to higher abundance of longer microtubules (Fig. 9G). Analysis of microtubule dynamics by simulating FRAP showed that asymmetry of microtubule dynamics was lower in the mutant (Fig. 9H). Thus, a lower microtubule nucleation rate in the model resembles phenotypes observed in the *mce4-1 mce5* mutant by partial loss of phragmoplast asymmetry and longer phragmoplast microtubules.

We tested the prediction of our model that a lower rate of microtubule nucleation in mce4-1 mce5 results in higher free tubulin abundance using the photo-convertible fluorescent protein EosFP fused to TuB2 (proTuB2:EosFP-TuB2). Stable transgenic lines in Col-0 were morphologically indistinguishable from Col-0 (Supplementary Fig. S6, A and B). Their root growth rate was also not affected (Supplementary Fig. S6, C and D). The experimental design is shown in Fig. 10A. Photoconversion in the designated region of the phragmoplast will switch the fluorescence of EosFP-TuB2 from green to red for both microtubules and free tubulin. Considering the high diffusion rate of free tubulin (Chang et al. 2005), the photoconverted fraction of tubulin will diffuse outside the converted region throughout the cell within 1 s after the photoconversion whereas microtubules that have a turnover rate of 18 s will be labeled only in the photoconverted



**Video 5.** A photoconversion experiment of the phragmoplast in Col-0 cells expressing *proTuB2:EosFP:TuB2* construct. The first three frames were recorded before the conversion. Only the bottom phragmoplast part was photo-converted.

area. The imaging data was used to measure free tubulin abundance relative to the polymerized microtubule fraction. Representative images of a phragmoplast before and after photoconversion are shown in Fig. 10B and Video 5. Quantification of the images revealed a higher tubulin/microtubules ratio in *mce4-1 mce5* than in Col-0 (Fig. 10C). Thus, free tubulin pool is higher in *mce4-1 mce5* than in the control.

### Discussion

### MACET paralogs function redundantly in decreasing the tubulin OFF rate

In vitro analysis of recombinant MACET4 demonstrated that MACET4 promotes microtubule nucleation at subcritical concentrations of tubulin and forms "cores" together with tubulin that nucleate microtubules (Schmidt and Smertenko 2019). Overexpression of MACET4 in N. benthamiana leaf pavement cells decreases the tubulin OFF rate (Schmidt and Smertenko 2019). Unfortunately, biochemical characterization of other MACET paralogs was impossible due to their insolubility in buffers compatible with microtubule assays. Therefore, we performed transient overexpression assays in N. benthamiana leaf pavement cells as an alternative using MACET4-GFP as a positive control and GFP-TuB6 as a negative control. In these experiments, all MACET paralogs caused a higher frequency of nondynamic microtubule ends, decreased the depolymerization rate, or both. These outcomes suggest that all MACET proteins function redundantly in lowering the tubulin OFF rate and can promote microtubule nucleation.

Another mechanism to promote microtubule nucleation is increasing the tubulin ON rate. MACETs proteins are unlikely to promote the tubulin ON rate because such proteins, e.g. MICROTUBULE ORGANIZATION 1 (MOR1) from the MAP215 family cause formation of longer microtubules in vitro (Hamada et al. 2004) and increase the microtubule polymerization rate in vivo (Kawamura and Wasteneys 2008). MACET4 causes formation of shorter microtubules in vitro and MACET paralogs collectively exhibit no consistent effect on microtubule growth rate in vivo. Furthermore, while proteins that increase the tubulin ON rate localize to the microtubule growing tips (Akhmanova and Steinmetz 2015), all Arabidopsis MACET paralogs accumulate only on the shrinking ends.

The conclusion about role of MACET in decreasing the tubulin OFF rate was tested by the long-term microtubule stability assays in cells expressing MACET1, MACET4, or MACET5 using the inhibitor of microtubule polymerization APM. We chose these proteins because MACET1 was suggested to destabilize microtubules by diminishing their interaction with the plasma membrane (Sasaki et al. 2017), MACET4 was proposed to destabilize microtubules by promoting severing through tethering of KATANIN to the microtubule lattice (Sasaki et al. 2019), and MACET5 is a close

paralog of *MACET4* with similar expression pattern. Microtubule destabilization or severing would cause decrease the abundance of microtubule polymers. However, none of the proteins tested here caused a drop in microtubule density or total microtubule length. On the contrary, microtubules were more stable in the presence of MACET1-GFP or MACET4-GFP. It was impossible to generate stable tobacco BY-2 cells or Arabidopsis transgenic lines expressing *MACET4* or *MACET5* under control of a strong constitutive promoter due to lethality or silencing. Therefore, the expression level of *MACET* plays an important role in preventing toxic hyper-stabilization of microtubules.

All MACET proteins with the exception of MACET6 caused microtubule wavering, although the frequency of these events was low considering the high protein abundance resulting from overexpression. Interestingly, the wavering events were accompanied by microtubule elongation. Thus, the wavering results from inhibition of collision-induced catastrophe whereby a microtubule continues to elongate upon encountering an obstacle instead of switching to catastrophe (Supplementary Fig. S3 E). This hypothesis is consistent with the ability of MACET proteins to decrease the tubulin OFF rate. The apparent lack of wavering in cells expressing MACET6 suggests that this protein allows for the loss of tubulin dimers from the microtubule tip upon encountering an obstacle.

### Effect of the GFP tag on MACET activity

We observed a positional effect of GFP on MACET activity. Indeed, the MACET4-GFP and MACET5-GFP fusions both suppressed microtubule depolymerization, whereas the GFP-MACET4 and GFP-MACET5 fusions did not. Furthermore, depolymerization of microtubules was slower for MACET4-GFP and GFP-MACET4 fusions, whereas microtubule depolymerization was slower in cells expressing GFP-MACET5 and faster in cells expressing MACET5-GFP. However, more microtubules survived treatment with APM in cells expressing MACET5-GFP than in cells expressing GFP-MACETS. On the contrary, GFP-MACET2 but not MACET2-GFP showed a lower frequency of dynamic microtubule ends. The position of GFP was also important for the activity of MACET3. The likely reasons for these outcomes are steric hindrance of GFP with MACET oligomerization, binding to microtubules, or both. Activity of untagged MACET4 resembled that of the MACET4-GFP fusion. Hence, GFP is not responsible for the role of MACET4 in decreasing the tubulin OFF rate and both MACET4-GFP and MACET5-GFP are active when the encoding expression cassette is driven by the native promoter. The ability of the proMACET4:MACET4-GFP construct to rescue the phragmoplast length phenotype of mce4-1 (Schmidt and Smertenko 2019) and the ability of proCORD4:CORD4-EYFP to rescue the phragmoplast length phenotype in macet4 macet5 double mutant (Sasaki et al. 2019) also supports the functional activity of the C-terminal fusions.

### Role of MACET in regulating phragmoplast microtubule dynamics and axial asymmetry

Biochemical assays with physiologically relevant concentrations of MACET4 and transient expression assays with MACET4 expressed under control of its native promoter revealed that MACET4 facilitates microtubule depolymerization by increasing the frequency of catastrophe in vivo and by suppressing rescue in vitro (Schmidt and Smertenko 2019). The modeling experiments in this work showed that a higher microtubule nucleation rate in the phragmoplast depletes the pool of free tubulin. It has been shown that free tubulin plays a critical role in regulating microtubule dynamics by determining the frequency of transition between catastrophe and rescue (VanBuren et al. 2005). A larger tubulin pool suppresses catastrophe, resulting in longer microtubules, whereas a smaller tubulin pool promotes catastrophe leading to shorter microtubules.

Proteins that increase the tubulin pool by promoting depolymerization or catastrophe cause microtubule polymerization indirectly. Loss of function for these proteins is expected to decrease both the tubulin pool and microtubule polymerization, while increasing the microtubule depolymerization rate. Consistent with this model, the knockout of the microtubule-depolymerizing gene Kinesin-13 in Physcomitrium patens caused a lower polymerization rate and an increased depolymerization rate in interphase cells (Leong et al. 2020). Lower frequency of catastrophe in an Arabidopsis knockout mutant of ARMADILLO REPEAT KINESIN1 was also accompanied by slower microtubule growth, suggesting a smaller tubulin pool (Eng and Wasteneys 2014). It is possible that depletion of the tubulin pool triggers microtubule depolymerization pathways that would replenish the pool. In this case, a lower tubulin OFF rate in cells overexpressing MACET would activate KATANIN-dependent severing and/or other microtubule depolymerization mechanisms.

Under physiological abundance levels, MACET4 does not decorate microtubules continuously, but forms puncta that co-localize with microtubule nucleation sites (Schmidt and Smertenko 2019 and this study). The puncta may be a mechanism to create a zone with an optimal environment for microtubule nucleation (Fig. 10D). In this case, the consequence of MACET on the tubulin OFF rate ceases once the microtubule extends beyond the puncta (Fig. 10D). Knockout of MACET4 and MACET5 leads to a higher tubulin pool in the phragmoplast that is expected to decrease the catastrophe rate and increase the rescue rate. This prediction is supported by two phenotypes of mce4-1 mce5: (1) the slower microtubule turnover rate in the midzone where most microtubule plus ends localize, whereas the turnover rate in the distal zone was not affected; and (2) longer phragmoplast. Overexpression of MACET also increases the stability of microtubules, but through a different mechanism—by lowering the tubulin OFF rate. The lower frequency of dynamic microtubule ends in cells overexpressing MACET paralogs indicates depletion of free tubulin pool below the level required for sustaining microtubule polymerization.

Increase of the free tubulin pool in mce4-1 mce5 abrogates phragmoplast axial asymmetry by slowing down microtubule turnover in the phragmoplast midzone. Axial asymmetry depends on the bias of microtubules plus ends orientation toward the cell plate (Euteneuer and McIntosh 1980). Our modeling approach demonstrates the importance of microtubule polarity for axial asymmetry (Smertenko et al. 2011). Another important factor is the dynamic behavior of microtubule plus ends. Blocking microtubule depolymerization with taxol increases axial asymmetry whereas inhibition of formins with the small molecule inhibitor SMIFH2 (1-(3-bromophenyl)-5-(furan-2-ylmethylene)-2-thioxodihydropyrimidine-4,6(1H,5H)-dione) decreases asymmetry (Smertenko et al. 2011; Zhang et al. 2021). The loss of axial asymmetry in mce4-1 mce5 is the consequence of slower microtubule depolymerization rate, which is most likely caused by a higher free tubulin pool. Axial asymmetry thus informs on changes of microtubule plus end dynamics and provides a useful parameter for functional characterization of phragmoplast proteins.

### MACET4 and MACET5 control the angle of branched microtubule nucleation

Branched microtubule nucleation takes place at the phragmoplast leading edge (Murata et al. 2013). This nucleation mechanism is common to all cell cycle stages and was proposed to sustain microtubule polarity in the arrays by amplifying microtubules of the same polarity (Petry et al. 2013). Consistent with this hypothesis, over 90% of phragmoplast microtubules share the same polarity (Euteneuer and McIntosh 1980). In addition to sustaining microtubule polarity, branching microtubules in the leading edge can probe the space and push against membrane compartments in the path of phragmoplast expansion. The importance of branched nucleation for sustaining the polarity of microtubule arrays necessitates mechanisms for precise control of the nucleation angle. We demonstrated that the branched nucleation at the phragmoplast leading zone occurred at 25° angles in wild-type plants and 40° in mce4-1 mce5 (Figs. 5F, G and 10D).

During interphase,  $\gamma$ -TuRC nucleates microtubules preferentially on the lattice of extant microtubules at an angle of approximately 40° (Murata et al. 2005; Kong et al. 2010; Hashimoto 2013). The augmin complex cooperates with  $\gamma$ -TuRC in maintaining the angle of branched nucleation during interphase (Lindeboom et al. 2013; Liu et al. 2014; Song et al. 2018) by recruiting  $\gamma$ -TuRC to the extant microtubule lattice (Hotta et al. 2012; Liu et al. 2014). Mutations in  $\gamma$ -TuRC alter the branched nucleation angle during interphase. For example, either overexpression or downregulation of *NEDD1* decreased the microtubule nucleation angle (Walia et al. 2014). The augmin complex does not control the angle but the frequency of the branched nucleation events.

Knockout of *AUG6* caused higher frequency of parallel microtubule nucleation with an angle of branched nucleation of 0° (Liu et al. 2014). Electron tomography studies showed a lack for parallel microtubule nucleation in the phragmoplast (Segui-Simarro et al. 2004; Austin et al. 2005). Parallel nucleation may compromise phragmoplast expansion rate by decreasing the expansion rate, and there are proteins that prevent these events. For example, it has been shown that mutation in the gene encoding the B" regulatory subunit of protein phosphatase 2A (*ton2*) caused higher frequency of parallel microtubule nucleation, but the angle of branched nucleation was not affected (Kirik et al. 2012).

In addition to the localization of MACET4-GFP and MACET5-GFP at the distal zone and control the angle of branched nucleation, MACET5-GFP also localizes in the nucleus. According to the NLStradamus algorithm (Ba et al. 2009), MACET5 has a nuclear localization sequence (NLS) between amino acids 495 and 502 with a probability of 0.9, whereas the highest probability of an NLS in MACET4 between amino acids 510 and 512 is 0.65. It has been shown that y-tubulin localizes to the nucleus in both plants and animals where it contributes to regulating gene expression (Sulimenko et al. 2022). One intriguing possibility is that MACET5 plays a role in gene regulation. The sequestering in the nucleus may contribute to decreasing microtubule nucleation by MACET5. Thus, MACET paralogs may be involved in cellular events that are unrelated to microtubule nucleation.

# MACET4 is a component of the cytokinetic microtubule nucleation network

Our work exposes both the complexity and nonlinearity of microtubule nucleation in the phragmoplast. Several experimental outcomes support the requirement of MACET4 for the functions of γ-TuRC and the augmin complex. First, MACET4 interacts with subunits of the γ-TuRC and augmin complexes, γ-tubulin and AUG7, respectively. Second, MACET4 functions as a tethering factor for AUG7. Third, when accumulating at physiological levels during interphase, MACET4 localizes to all microtubule nucleation sites (Schmidt and Smertenko 2019). Fourth, *mce4-1 mce5* and *aug7-1* mutants have longer phragmoplasts and a greater nondynamic fraction of microtubules than the wild type. Fifth, the *mce4-1 mce5 aug7-1* triple mutant leads to embryo or early seedling death.

The animal augmin complex binds to microtubules through its evolutionarily nonconserved subunit Hice1 that corresponds to plant AUG8 (Wu et al. 2008). AUG8 together with AUG2, AUG7, and AUG6 form the backbone of the augmin complex to which the other four subunits bind (Gabel et al. 2022). AUG7 lacks microtubule-binding capacity in animals (Wu et al. 2008; Gabel et al. 2022) and in plants (our study). According to structural data of animal augmin complex, the microtubule-binding region of AUG8 is located in its N-terminal unstructured region within the V-shaped

head. The N terminus of AUG7 locates proximally to the N terminus of AUG8. Interpreting the *aug7-1* phenotype and the interaction of AUG7 with MACET4 is complicated by the lack of structure of plant augmin complex and by the fact that primary structure of plant and animal AUG7 is not conserved (Hotta et al. 2012). MACET4 could enhance the association of the augmin complex with microtubules by binding to the N-terminal region of AUG7 near the main microtubule binding site of the augmin complex. A similar enrichment of MACET4-GFP at the phragmoplast distal end in Col-0 and *aug7-1* demonstrates that AUG7 is not required for MACET4 localization.

The requirement of tubulin or microtubules for the interaction between MACET4 and γ-tubulin but not between AUG7 suggests that MACET4 plays several distinct roles in microtubule nucleation. For example, MACET4 stabilized interactions between y-tubulin and tubulin dimers during early stages of microtubule nucleation and crosslink γ-tubulin with the microtubule lattice (Fig. 10D). Comparison of aug7-1 and mce4-1 mce5 shows only a partial functional overlap for AUG7, MACET4, and MACET5. In particular, similar branched microtubule nucleation angles in aug7-1 and Col-0 suggests the redundancy of AUG7 in branched microtubule nucleation. Animal cells have an augmin-independent mechanism for branching nucleation via SS Nuclear Autoantigen 1 (SSNA1) (Basnet et al. 2018). MACET4 and SSNA1 show similar activity in vitro by producing branched microtubules (Schmidt and Smertenko 2019). Hence, MACET4 may sustain branched nucleation in the absence of AUG7 independently or through interaction with γ-tubulin. Some association of AUG7 with phragmoplast microtubules in mce4-1 mce5 highlights the redundancy of MACET4 and MACET5 in tethering the augmin complex to microtubules. This role may also be filled by the other MACET paralogs or AUG8.

Axial asymmetry was not affected in *aug7-1*. As axial asymmetry depends on microtubule nucleation, this outcome points to the unique contribution of MACET for generating this bias and that AUG7 may not control microtubule nucleation rate. However, greater phragmoplast length and the immobile fraction of microtubules in both *mce4-1 mce5* and *aug7-1* suggest that AUG7 can destabilize microtubules independently of microtubule nucleation. The phragmoplast expansion rate in *mce4-1 mce5* was not affected, whereas phragmoplast expansion was slower in *aug7-1*. Thus, the functions of AUG7 and MACET in cytokinesis appear to be only partially redundant.

In conclusion, understanding the mechanisms of microtubule nucleation and assigning functions to the individual components play a critical role in constructing an accurate model of plant cytokinesis. Our work advances the modeling efforts by introducing several essential rules. First, all MACET proteins decrease the tubulin OFF rate and thus may play a redundant role in microtubule nucleation. Second, MACET4 and MACET5 contribute to microtubule depolymerization indirectly by depleting the pool of free tubulin. Third, the

free tubulin pool is a crucial parameter for phragmoplast axial asymmetry and phragmoplast architecture. Fourth, MACET4 and AUG7 function in controlling phragmoplast length and microtubule stability. Fifth, MACET4 and MACET5 maintain phragmoplast axial asymmetry and decrease the angle of branched microtubule nucleation. Sixth, MACET4 tethers AUG7 to phragmoplast microtubules, but AUG7 is not required for MACET4 localization. The next important steps in this direction will be (1) determining mechanisms responsible for spatial control of balance between branched and nonbranched microtubule nucleation events in the phragmoplast; (2) identifying other structural and signaling components in the distal zone and understanding their functions in regulating MACET proteins; and (3) exploring the crosstalk between microtubule abundance and activity of microtubule depolymerization pathways.

### Materials and methods

#### **Constructs**

Accession number for all genes used in this study is provided in Supplementary Table S3. The target sequence for CRISPR/ Cas9-mediated gene editing of MACET5 was selected manually and the protospacer adjacent motif (PAM) was designed according to published protocols (Steinert et al. 2015). The complementary protospacer oligonucleotides MACET5-Sa-sgRNA-F-TS and MACET5-Sa-sgRNA-R-TS (Supplementary Table S4) were annealed and ligated into the pEN-Sa\_Chimera vector (Steinert et al. 2015) using a previously described protocol (Liu et al. 2015). The confirmed entry clone was recombined with the modified binary vector pDe-Sa-CAS9 (Steinert et al. 2015) via Gateway LR recombination (Thermo Fisher Scientific). This vector was provided by John Sedbrook. The resulting entry and destination clones were verified by Sanger sequencing with primer SS42 (Supplementary Table S4; Schiml et al. 2016).

To produce proTuB2:mNeonGreen-TuB2, proTuB2:EosFPproTuB2:mScarlet-TuB2, proAUG7:AUG7-TuB2, and mNeonGreen, constructs, modules were created for the Arabidopsis TuB2 promoter, N-terminal mNeonGreen, N-terminal mScarlet, N-terminal EosFP, the Arabidopsis TuB2 genomic sequence, the Arabidopsis AUG7 promoter, the Arabidopsis AUG7 genomic sequence, and C-terminal mNeonGreen using primers pGGA\_pAtTUB2\_F/pGGA\_ pGGB\_NG\_linker\_F/pGGB\_NG\_linker\_R, pAtTUB2\_R, pGGB\_mScarlet\_F/pGGB\_mScarlet\_linker\_Rnew, pGGB\_EO SFP\_linker\_F/pGGB\_EOSFP\_linkerNew\_R, pGGC\_AtTUB2-3\_F/pGGC\_AtTUB2Stop\_R, pGGA\_pAtAUG7\_F/pGGA\_pAt pGGC\_AtAUG7\_noSTOP\_F/pGGC\_AtAUG7\_no STOP\_R, and pGGD\_neonGreen NEW\_F/pGGD\_ neonGreen NEW\_R, respectively (Supplementary Table S4). The modules were assembled in the pGGZ003 destination vector together with the resistance cassette for hygromycin B (for proTuB2: mNeonGreen) or kanamycin (for proTuB2:EosFP-TuB2 and proAUG7:AUG7-mNeonGreen) using GreenGate technology (Lampropoulos et al. 2013).

For simultaneous expression of proUBQ10:mNeonGreen and proUBQ10:MACET4 from the same backbone, modules were created for mNeonGreen and MACET4 using primers pGGB\_nG\_linker\_F/pGGD\_nG\_R and pGGC\_Macet4\_F/pGGC\_Macet4\_R, respectively (Supplementary Table S4). The mNeonGreen and MACET4 modules were assembled into separate cassettes using intermediate vectors pGGM000 and pGGN000, respectively. Subsequently, the two cassettes were assembled in the pGGZ003 destination vector together with the hygromycin B resistance cassette using GreenGate technology (Lampropoulos et al. 2013).

The binary vector pUBN or pUBC (Grefen et al. 2010) harboring the sequence encoding GFP for N-terminal or C- terminal fusions were used for expression in *N. benthamiana*. The full-length *MACET* coding sequence was amplified by Phusion PCR from Arabidopsis Col-O leaf first-strand cDNA using gene-specific primers for each *MACET* family member. Gateway extensions corresponding to *attB1* and *attB2* sites were added to forward and reverse primers, respectively and named MACETn FWDattB1 and REVattB2 (Supplementary Table S4).

For the native promoter: GUS cassettes, the following genomic DNA regions were selected as potential promoters: 3,022 bp starting 10 bp upstream from the transcription start site (ATG) (MACET2), 1,644 bp starting 8 bp upstream from the ATG (MACET3), 2,381 bp up to the ATG (MACET4), 3,152 bp starting 4 bp upstream from the ATG (MACET5), 3,201 bp up to the ATG (MACET6), 3,148 bp starting 10 bp upstream from the ATG (MACET7). Primers were named as follows: MACETnProFWDattB1 and MACETnProREVattB2 (Supplementary Table S4). The promoter regions were individually cloned into Gateway vector pBI101G upstream of the GUS reporter gene.

The construct *proMACET4:MACET4-GFP* was generated as previously described (Schmidt and Smertenko 2019). To generate C-terminal GFP-fusions, a 2- to 4-kb region upstream of the ATG and the genomic DNA sequence of *MACET5 or MACET7* were cloned into the gateway vector pMDC107 (Curtis and Grossniklaus 2003) using primers MACETnProFWDattB1 and MACETnREVattB2 to generate constructs *proMACET5:MACET5-GFP* and *proMACET7: MACET7-GFP*.

All transient and stable genetic lines and mutants generated in this work are listed in Supplementary Table S5.

# Plant growth, transformation, and identification of transgenic lines

All Arabidopsis lines used in this study were produced in the Col-0 accession. Seeds stratification was performed at 4 °C for 48 h and plants were grown at 22 °C with 16-h light/8-h dark photoperiod at 100 to 150  $\mu$ mol/m²/sm daylight spectrum bulbs. *N. benthamiana* plants were grown at 21 °C with 16-h light/8-h dark photoperiod at 150 to

 $200~\mu mol/m^2/s$  daylight spectrum bulbs. For the imaging experiments, surface-sterilized seeds were sown on half-strength Murashige and Skoog (MS) medium solidified with 1% (w/v) agar and stratified for 2 d at 4 °C and grown vertically under the conditions described above. Plants were transformed by the floral dip method (Clough and Bent 1998) in Col-0. Imaging was performed on the  $T_2$  or  $T_3$  generations.

The T-DNA insertion mutant *aug7-1* (seed stock SK18263) was obtained from the Arabidopsis Biological Resource Center (ABRC) and genotyped using published procedures (Hotta et al. 2012). The *proMACET4:MACET4-GFP* or *proTuB2:mNeonGreen-TuB2* transgene was introduced into the *aug7-1* mutant background through crossing. *proAUG7: AUG7-mNeonGreen* was introduced into Col-0 or *macet4-1 macet5* through transformation as above. *proTuB2: mNeonGreen-TuB2, proTuB2:EosFP-TuB2* and *proTuB2: mScarlet-TuB2* were introduced into Col-0 through transformation via floral dipping.

For CRISPR/Cas9 gene editing, the construct containing the MACET5-specific single guide RNA was transformed in Agrobacterium (Agrobacterium tumefaciens) strain GV3101 before being transformed into mce4-1 (Schmidt and Smertenko 2019) as above. Primary transformants (T<sub>1</sub>) (n = 20) were selected on agar plates with half-strength MS-medium containing 20 mg/L hygromycin B and 100 mg/L timentin, transplanted into soil and subjected to heat stress (LeBlanc et al. 2018).  $T_2$  (n = 10) and  $T_3$ (n = 20) progeny were checked for 3:1 segregation on selection medium (20 mg/L hygromycin B) to identify lines lacking the transgene. Seedlings, which were growing slowly on plates supplemented with 20 mg/L hygromycin B, were transferred to a plate with nonselective half-strength MS medium for recovery and then to soil. T<sub>2</sub> and T<sub>3</sub> generation plants were examined for targeted gene modification via Sanger sequencing of PCR products amplified using primers cM5\_FWD and cM5\_REV spanning the target sequence. T<sub>3</sub> lines were additionally screened for the lack of Cas9 gene via PCR using primers Cas9-Sa-F and Cas9-Sa-R (Supplementary Table S4). All imaging experiments were performed on the  $T_2$  and  $T_3$  generations.

#### Live cell imaging

Transient expression in *N. benthamiana* leaf pavement cells was performed using previously published procedures (Smertenko et al. 2008). Briefly, *A. tumefaciens* strain GV3101 was transformed with the constructs of interest. Bacterial cultures were grown overnight in 3.0 mL of YEB at 30 °C, 200 rpm until OD<sub>600</sub> nm reached 0.6 to 1.0, the cells were collected by centrifugation at  $3,000 \times g$  for 5 min and washed two times with infiltration medium composed of 10 mm MES pH 5.6, 10 mm MgCl<sub>2</sub>, and 200  $\mu$ M Acetosyringone. Bacterial suspensions were mixed in the ration 1:1 (v/v) with a culture carrying *p19* and injected into the *N. benthamiana* abaxial leaf side. The abaxial sides of infiltrated leaves were imaged 2 to 5 d after infiltration. For

drug treatment, a 2 mm × 2 mm was cut from leaves and soaked in 20 µM APM or 2% (v/v) DMSO solution for 75 min before imaging. Roots were mounted under a slice of solid half-strength MS medium on a round 3-cm diameter microscope dish. For cell membrane staining, Arabidopsis roots were incubated in 1  $\mu$ M FM4-64 for 10 min, and then mounted on the dish as above. Images were collected using a Leica SP8 confocal laser scanning microscope equipped with a 40× NA1.3 oil immersion objective. GFP was excited by 488 nm and FM4-64 was excited by 561 nm wavelength. All time-lapse images were collected in a single optical plane with a pinhole size of 1.5. The images of cells in the APM-treatment experiments are maximum projections of an image stack of 1-µm optical sections acquired with a pinhole size of 1. The images of the phragmoplast were recorded at pinhole size 0.4 to 0.6.

EosFP photoconversion was achieved with a 1.5-s pulse of a 405-nm laser set at 2% power. The objective was as above and the pinhole was set to 1 Airy unit. The photoconverted signal was imaged with excitation at 561 nm and an emission window of 570 to 640 nm. The photobleaching step of the FRAP experiments was performed with a 2 to 2.6-s pulse of the 488-nm line from an argon laser at 20% power. The signal recovery was imaged using the 488-nm line of the argon laser at 0.5% power for excitation and the emission window was 495 to 590 nm; the pinhole was set to 0.6 airy unit and the image acquisition rate was of 2 to 2.6 s per frame. The signal recovery was quantified using ImageJ (Schindelin et al. 2012) and the turnover rates were calculated using single-exponential fit (Chang et al. 2005). Imaging of microtubule nucleation at the phragmoplast leading edge was performed using the same microscope settings as in FRAP experiments.

### Image analysis and statistics

The xy drift was adjusted using the StackReg plug in for ImageJ (Thévenaz et al. 1998). Microtubule density was measured using ImageJ. A minimum of 3 square areas were chosen per cell, with the squares at the distal edge of the lobe. Individual microtubules within the squares were traced to measure the total length and number of microtubules per area. Statistical analysis was performed using Graphpad Prism 5.0.

Kymographs were constructed using the ImageJ kymograph plugin. For kymographs tracking puncta particles, microtubules fragments were traced with the segmented line tool between intersecting microtubules to avoid counting an intersection as a particle. Particles that shifted were traced for rate analysis; appearing or disappearing particles were not counted as stable or shifting. Microtubule dynamics parameters were measured on the kymographs by exporting x and y pixel coordinates of the microtubule events and translating the coordinates into length and time values. These values were used to calculate the growth and shrinkage rates. Individual events of the particle behavior were counted manually. Charts and statistical analyses were performed using GraphPad Prism 5.0.

Pixel intensity was measured using the Plot Profile function in Imagel. Lines were traced to cover MACET signal in cyto-kinetic cells spanning the daughter nuclei or cortical microtubules. Growing and shrinking microtubule ends were colored using frame subtraction following a published procedure (Lindeboom et al. 2013) with the time difference between the frames  $\sim$ 18 and 19 s.

Microtubule nucleation in phragmoplast asymmetry

The ratio between free tubulin and microtubules was calculated using time-lapse image sequences recorded in cells harboring proTuB2:EosFP-TuB2 using the following equation:  $(I^{ROI4} - I^{ROI2})/(I^{ROI3} - I^{ROI1})$ , where I is signal intensity in the corresponding four regions of interest (ROIs) shown in Fig. 10A.

Statistical analysis and construction of charts were performed using GraphPad Prism. Statistical analysis of differences between control and treatments was performed using two-tailed unpaired t-test. All error bars unless stated otherwise represent standard deviation.

### Beta-glucuronidase assays

Seedlings were grown on half-strength MS medium solidified with 0.8% (w/v) agarose; mature plants were grown on soil. The desired plant tissue was harvested and placed immediately in 90% (v/v) acetone, enough to cover the plant tissue, in microfuge tubes or glass test tubes on ice. The tissues were incubated at room temperature for 20 min. All samples were washed in chilled staining buffer (50 mm NaPO<sub>4</sub>, 0.2% Triton X-100 (v/v), 1 mm potassium ferrocyanide, 1 mm potassium ferricyanide) and vacuum-infiltrated on ice for 15 min. The staining buffer was replaced with staining buffer containing 2 mm X-Gluc and vacuum-infiltrated on ice for 15 to 20 min. Samples were incubated overnight at 37 °C in the dark. Staining buffer was removed and tissue was washed in a series of ethanol washes: 20%, 35%, and 50% (all v/v) ethanol at room temperature for 30 min each. Samples were incubated in fixative solution (50% EtOH (v/v), 3.7% (w/v) formaldehyde, 5% (v/v) acetic acid) for 30 min at room temperature. The fixative was removed and samples were stored in 70% (v/v) ethanol at 4 °C. If necessary, chlorophyll was removed with leaf-clearing solution containing 6 M urea, 30% (v/v) glycerol, 0.1% (v/v) Triton X-100 for up to 4 wk at 4 °C (Weigel and Glazebrook 2002).

# BY-2 cell culture and cell cycle synchronization and total cell protein extraction

*N. tabacum* BY-2 cells were grown in liquid MS medium containing 200 mg L<sup>-1</sup> KH<sub>2</sub>PO<sub>4</sub>, 3% (w/v) sucrose, and 0.2 mg L<sup>-1</sup> 2,4-dichlorophenoxyacetic acid (2.4-D), pH 5.8, at 25 °C in the dark, with shaking at 150 rpm (Nagata et al. 1981). Cells were subcultured every 7 d by transferring 1 mL of old culture into 60 mL of fresh medium. For the cell cycle synchronization experiments, 6 mL of a 7-d-old BY-2 culture was inoculated into 60 mL of fresh medium containing 3  $\mu$ M aphidicolin, and incubated for 24 h under normal growth conditions. Then cells were washed

intensively in several changes of 30% (w/v) sucrose solution (total 1.5 L) in a sintered glass funnel to remove aphidicolin and then incubated in 60 mL of fresh medium for 4 to 6 h. Propyzamide was added to a final concentration of 5  $\mu$ m. After 4 h, the accumulation of metaphase cells was monitored every hour by staining cell aliquots using a modified 4′,6-diamidino-2-phenylindole (DAPI) stain (Smertenko et al. 2016). Once the metaphase index started to plateau (ca. 5 to 7 h), propyzamide was removed with washes in 30% (w/v) sucrose as described above and the transition of cells to telophase was monitored every 40 min. Cells were collected by filtration when the frequency of telophase cells reached 40%, flash-frozen in liquid N<sub>2</sub>, and stored at -80 °C.

## Recombinant protein production, pull-down, and biochemical assays

Recombinant MACET4 and AtMAP65-1 were produced in *E. coli* strain BL21 (DE3) Rosetta-2 and purified using Ni-NTA affinity chromatography according to the published procedure (Schmidt and Smertenko 2019). The proteins were further purified using a Superdex 200 Increase column and Äkta FPLC and dialyzed overnight at 4 °C against buffer containing 20% (v/w) glycerol, 50 mm PIPES-KOH, pH 6.8, 2 mm EGTA, 2 mm MgSO<sub>4</sub>, 10 mm DTT, and 50 mm KCl.

To prepare protein extract from tobacco BY-2 cells, frozen material was ground to a fine powder and mixed with Microtubule Stabilization Buffer (MTSB; 50 mm PIPES, pH 6.8, 2 mm EGTA, 2 mm MgSO<sub>4</sub>) containing 20% (v/v) glycerol and protease inhibitors (1  $\mu$ g/mL each of leupeptin and pepstatin A, 0.05  $\mu$ g/mL MG132, 0.01  $\mu$ g/mL E10, and 1 mm PMSF). The powder was homogenized on ice and centrifuged at 270,000 × g for 10 min at 4 °C to remove cellular debris. The supernatant was collected avoiding the vesicle fraction on the surface and centrifuged at 270,000 × g for 30 min at 4 °C.

Microtubules were polymerized using a mixture of ATTO488-labeled tubulin and unlabeled cow brain tubulin at a molar ratio 1:5 at 37 °C for 10 min and stabilized with 20  $\mu$ M taxol. The quality of microtubules was verified under a TIRF microscope. Then 80  $\mu$ L of microtubules were mixed with recombinant MACET4 at a molar ratio MACET4:microtubules of 1:5, and with 1 mg of total BY-2 protein extract. The mixture was layered over 1 mL of a 60% (v/v) glycerol cushion in MTSB buffer and centrifuged for 10 min at 4 °C and 350,000 × g. The pellet was washed with distilled water, dissolved in 50  $\mu$ L of SDS-PAGE sample buffer and run for 1 cm on a 10% (w/v) SDS-PAGE gel. The region of the gel containing proteins was cut in four horizontal sections and each section was stored in 1% (v/v) acetic acid.

To make cores, 5  $\mu$ m ATTO-488 labeled tubulin (molar ratio of labeled to unlabeled tubulin 1:4) was mixed with 1  $\mu$ m MACET4 in 20  $\mu$ L, incubated on ice for 3 min, then in a 37 °C water bath for 10 min. The quality of cores was verified under a TIRF microscope. Then cores were mixed with BY-2 protein extract and binding proteins were purified as described above for microtubules. Pull-down assays were repeated and liquid

chromatography tandem mass spectrometry and peptide analysis of the isolated proteins were performed by Southern Alberta Mass Spectrometry Facility of Calgary University.

In vitro microtubule dynamics assays were performed according to the published procedures (Schmidt and Smertenko 2019).

### Protein-affinity chromatography

Recombinant MACET4, MAP65-1 (At5g55230), Brachypodium distachyon MAP20 (Bradi4g27760; XP\_0035 76401; Smertenko et al. 2020) were produced as above with the exception of using Ni-Affinity chromatography in buffer containing 4 M guanidine HCl, 150 mM NaCl, and 100 mM HEPES, pH 7.0. The proteins were coupled to Thermo Scientific Pierce NHS-activated agarose resin according to the manufacturer's instructions. The column was equilibrated with 6 mL of Wash Buffer (100 mm NaCl, 100 mm HEPES, pH 7.4). BY-2 protein extract was prepared as above but with the extraction buffer 0.2% (v/v) Triton X-100, 100 mm NaCl, 100 mm HEPES, pH 7.4, protease inhibitors 1 μg/mL each of leupeptin and pepstatin A, 0.05 µg/mL MG132, 0.01 µg/mL E10, and 1 mm PMSF. The extract was loaded onto the resin, and incubated for 2 h on ice. Weakly binding and unbound proteins were removed with three washes in Wash Buffer. Bound proteins were eluted with 4 M NaCl, 100 mm HEPES, pH 7.4. Affinity chromatography purification was repeated and liquid chromatography-tandem mass spectrometry and peptide analysis was performed by Southern Alberta Mass Spectrometry Facility of Calgary University.

# Transient expression and bimolecular fluorescence complementation assays

The full-length coding sequences of CLASP, AUG7, γ-tubulin (TUBG1), MAD2, and RabA4A were individually amplified from Arabidopsis Col-0 leaf cDNA via PCR using corresponding primers (Supplementary Tables S1 and S4). The PCR products were cloned into the pDONR207 vector using Gateway technology (Invitrogen, ThermoFisher Scientific, USA), verified by Sanger sequencing, and introduced into binary vectors. pSITE-nEYFP-N1 was used to generate N-terminal fusions of the following proteins, CLASP, AUG7, TUBG1, MAD2, and RabA4A, to the N-terminal half of enhanced yellow fluorescent protein (EYFP). The C-terminal fusions to the N-terminal or C-terminal half of EYFP were constructed using pSITE-nEYFP-C1 (for MACET4) and pSITE-cEYFP-C1 (for MACET4, CLASP, AUG7, TUBG1, MAD2, and RabA4A); (Martin et al. 2009). The constructs were transformed into Agrobacterium strain GV3101. Agrobacterium cultures were grown as described previously (Schmidt and Smertenko 2019) except that the final OD<sub>600</sub> of the bacterial suspension for infiltration was adjusted to 0.6. Cell cultures harboring pSITE-nEYFP-MACET4 or pSITE-cEYFP-MACET4 were mixed with cultures harboring either CLASP, AUG7, TUBG1, MAD2, or RabA4A cloned into pSITE-nEYFP-N1or pSITE-cEYFP-C1 and p19 at the ratio 1:1:0.5 (v/v/v). For the negative controls, cells harboring pSITE-cEYFP-MACET4 were mixed with cells harboring either *AUG7* and *TUBG1* cloned into pSITE-nEYFP-N1 and p19 at the ratio 1:1:0.5 (v/v/v). The leaves of *N. benthamiana* plants were infiltrated as described in Schmidt and Smertenko (2019). Leaves were imaged at 3 to 5 d after infiltration using a Leica SP8X confocal microscope.

### Phragmoplast microtubule dynamics model

The model was built using the C++ language and utilizes a Monte Carlo approach to simulate the deterministic relationship of microtubule dynamics and available tubulin within the cell. Parameters of the model are shown in Supplementary Fig. S9 A and listed in Supplementary Table S2. The code is available at the following GitHub link: https://github. com/matthewhickey98/PhragmoplastSimulator. For the purposes of our model, a fixed number of microtubule nucleation sites (seeds) were distributed through phragmoplast following a distribution determined by a given position in the phragmoplast of a mean value and standard deviation (Seed\_Mean and Seed\_SD). The seed locations remained constant throughout the simulation. Directionality of microtubule growth was set to 95% (frac\_grow\_in) toward the midzone and 5% (frac\_grow\_out) toward the distal edge based on published data (Euteneuer and McIntosh 1980). The distribution of microtubule nucleation sites is shown in Supplementary Fig. S9, B and C.

At any given time, a microtubule can be in one of three basic states: growing, paused, or shrinking (Supplementary Fig. S9 A). Transition between the states is described by parameters  $r_{gs}$ ,  $r_{sg}$ ,  $r_{pg}$ ,  $r_{ps}$ ,  $r_{gp}$  and  $r_{sp}$  listed in Supplementary Table S2. The polymerization and depolymerization rates of the microtubule are, respectively,  $r_{polym}$  and  $r_{depolym}$ . In addition, we introduced two phragmoplast-specific microtubule rates (Supplementary Fig. S9 A). First, the transition rate from pause to shrinking at the cell plate  $(r_{ps\_CP})$  once the x coordinate of a growing microtubule tip is less than or equal to CP\_XMAX. The purpose of this rate is to stabilize microtubule plus ends at the midzone in agreement with two studies: (1) the morphology of the plus tips proximal to the midzone corresponds to the stable state (Austin et al. 2005); and (2) some microtubules survive treatment with the inhibitor of microtubule polymerization propyzamide for 3 min (Murata et al. 2013). Second, the transition from pause to shrinking at the distal zone  $(r_{ps})$  once the x coordinate of growing microtubule tips is greater than or equal to DZ\_X\_MIN. This parameter creates bias in the destabilization in this region to prevent microtubules growing toward the distal zone from reaching outside of the phragmoplast.

The number of microtubules in the simulation was set to 1,000. Initially, all microtubules are nucleated to have a random length between 0 and  $L0 = 0.805 \, \mu \text{m}$ . When a microtubule nucleation site becomes empty due to catastrophe, it will be reseeded at the  $r_{\text{reseed}}$  rate. This rate depends on the location of the nucleation site (seed) and decreases linearly as the location approaches the distal edge. The slope

and y intercept of this parameter are determined by the reseed\_slope and reseed\_b parameters. Immediately after nucleation, a microtubule is placed in the growing state and subjected to the same calculations as other microtubules.

Microtubule polymerization and depolymerization are stochastic events governed by a Poisson distribution with a specific rate for each state transition (the parameters  $r_{\text{polym}}$ ,  $r_{\text{depolym}}$ ,  $r_{\text{gs}}$ ,  $r_{\text{reseed}}$ ,  $r_{\text{pg}}$ ,  $r_{\text{ps}}$ ,  $r_{\text{gp}}$ ,  $r_{\text{sp}}$ ,  $r_{\text{ps}}$ ,  $r_{\text{$ 

The amount of available tubulin in the cell is determined by the parameter tubulin\_density. This parameter is updated after each event, defined as a switch between all possible states for a given microtubule. The tubulin\_density parameter affects the rates  $r_{\rm gs}$ ,  $r_{\rm sg}$ ,  $r_{\rm pg}$ ,  $r_{\rm ps}$ ,  $r_{\rm gp}$ ,  $r_{\rm sp}$ , and  $r_{\rm polym}$ . During each event, relative tubulin (tubulin\_density\_current/tubulin\_density\_initial) is calculated. The rates that promote growth ( $r_{\rm sg}$ ,  $r_{\rm pg}$ ,  $r_{\rm sp}$ , and  $r_{\rm polym}$ ) are multiplied by this ratio whereas the rates that promote catastrophe are divided by this rate ( $r_{\rm gs}$ ,  $r_{\rm ps}$ , and  $r_{\rm gp}$ ). The net effect of these changes is promoting catastrophe when free tubulin is exhausted and promoting rescue when there is more tubulin.

The model is first run for 300 units of time (s) to let it relax to a steady state. The microtubules in the FRAP area, defined as rectangles of size 1.1  $\mu$ m  $\times$  4  $\mu$ m, are then bleached. The fluorescent signal on the microtubules in the bleached region is set to zero, but their behavior is governed by the same rules as prior to bleaching. The average luminosity of the microtubules is calculated by adding the total amount of luminous lines that are drawn by the microtubules. The luminosity of the images is scaled to be between 0 and 1 based on the single most luminous pixel.

We performed many simulations with a wide range of parameter values to determine how the parameters of microtubule dynamics along with the seeding rate and the availability of tubulin affected the recovery of microtubules after bleaching, the length of microtubules, and the shape of the kymograph. Starting with known rates, we were able to fit the simulation parameters to produce results that were seen in the control. Next, various parameters were changed and tuned to account for the observations of the *macet* mutants. The microtubule length distribution was obtained by computing an average of 10 simulations of 1,000 microtubules each.

### Statistical analysis

Statistical analyses were performed as described in each figure legend. Statistical data are provided in Supplementary Data Set S1.

#### **Accession numbers**

Sequence data from this article can be found in the GenBank/EMBL data libraries under accession numbers listed in Supplemental Table 3.

### **Acknowledgments**

The authors are grateful to Anna Matveeva, Zoe Ferguson, and Peter Coggan for help with GUS staining, Hunter Whitlock, Bethlehem Yohannes, and Stephanie Denton (Washington State University) for help with measuring microtubule dynamics, to Drs. Steve Simasko and Gary Wayman (Washington State University) for access to confocal microscopes, Dr. Laurent Brechenmacher, University of Calgary, for help with proteomics analysis, Dr. John Sedbrook, University of Illinois, for the pEN-Sa\_Chimera and pDe-Sa-Hyg vectors. This work was supported by NSF-CAREER award #1751204 to A.S.

#### **Author contributions**

Conceptualization: A.S., B.M.A.G.P.; Investigation: S.M.S., A.P., T.S., M.H., A.S.; Software: M.H., B.M.A.G.P., data analysis: S.M.S., M.H., A.S., A.P.; writing of original draft: S.M.S., A.P., T.S., M.H., A.S.; reviewing and editing: S.M.S., A.P., T.S., M.H., B.M.A.G.P., A.S.; funding acquisition: A.S.

### Supplementary data

The following materials are available in the online version of this article.

**Supplementary Figure S1.** Analysis of microtubule behavior in *N. benthamiana* leaf pavement cells expressing *MACET* paralogs.

**Supplementary Figure S2.** Effect of untagged MACET4 on microtubule dynamics in *N. benthamiana* leaf pavement cells.

**Supplementary Figure S3.** GUS activity in Arabidopsis transgenic lines expressing the GUS reporter under the control of the MACET2, MACET3, or MACET6 promoter.

**Supplementary Figure S4.** GUS activity in Arabidopsis transgenic lines expressing the GUS reporter under the control of the MACET5 or MACET7 promoter.

**Supplementary Figure S5.** Characterization of the *mce4-1 mce5* phenotype.

**Supplementary Figure S6.** Characterization of Arabidopsis  $\beta$ 2-tubulin marker lines.

**Supplementary Figure S7.** Analysis of Arabidopsis and to-bacco BY-2  $\beta$ 2-tubulin marker lines.

**Supplementary Figure S8.** Characterization of MACET4-interacting proteins.

**Supplementary Figure S9.** Model of phragmoplast microtubule dynamics.

**Supplementary Table S1.** Summary of MACET4 interactors.

**Supplementary Table S2.** Parameters used in the simulation of the phragmoplast microtubule dynamics.

**Supplementary Table S3.** Accession number of all genes used in this study.

**Supplementary Table S4.** List of primers and oligonucleotides used in this study.

**Supplementary Table S5.** Mutants and transgenic material used in this study.

**Supplementary Data Set S1.** Summary of statistical analyses in this study.

Conflict of interest statement. None declared.

### Data availability

Data available on request.

### References

- Abe T, Hashimoto T. Altered microtubule dynamics by expression of modified alpha-tubulin protein causes right-handed helical growth in transgenic Arabidopsis plants. Plant J. 2005:43(2):191–204. https://doi.org/10.1111/j.1365-313X.2005.02442.x
- **Akhmanova A, Steinmetz MO**. Tracking the ends: a dynamic protein network controls the fate of microtubule tips. Nat Rev Mol Cell Biol. 2008:9(4):309–322. https://doi.org/10.1038/nrm2369
- Akhmanova A, Steinmetz MO. Control of microtubule organization and dynamics: two ends in the limelight. Nat Rev Mol Cell Biol. 2015:16(12):711–726. https://doi.org/10.1038/nrm4084
- **Alfaro-Aco R, Thawani A, Petry S.** Biochemical reconstitution of branching microtubule nucleation. Elife. 2020:**9**:e49797. https://doi.org/10.7554/eLife.49797
- **Asada T, Sonobe S, Shibaoka H.** Microtubule translocation in the cytokinetic apparatus of cultured tobacco cells. Nature. 1991:**350**(6315):238–241. https://doi.org/10.1038/350238a0
- Austin JR II, Seguié-Simarro JM, Staehelin LA. Quantitative analysis of changes in spatial distribution and plus-end geometry of microtubules involved in plant-cell cytokinesis. J Cell Sci. 2005:118(17): 3895–3903. https://doi.org/10.1242/jcs.02512
- **Ba ANN, Pogoutse A, Provart N, Moses AM**. NLStradamus: a simple Hidden Markov Model for nuclear localization signal prediction. BMC Bioinform. 2009:**10**. https://doi.org/10.1186/1471-2105-10-202
- Bajer A. Fine structure studies on phragmoplast and cell plate formation. Chromosoma. 1968:24(4):383-417. https://doi.org/10.1007/BF00285016
- Basnet N, Nedozralova H, Crevenna AH, Bodakuntla S, Schlichthaerle T, Taschner M, Cardone G, Janke C, Jungmann R, Magiera MM, et al. Direct induction of microtubule branching by microtubule nucleation factor SSNA1. Nat Cell Biol. 2018:20(10): 1172–1180. https://doi.org/10.1038/s41556-018-0199-8
- Chang HY, Smertenko AP, Igarashi H, Dixon DP, Hussey PJ. Dynamic interaction of NtMAP65-1a with microtubules in vivo. J Cell Sci. 2005:118(14):3195–3201. https://doi.org/10.1242/jcs.02433
- **Clough SJ, Bent AF**. Floral dip: a simplified method for Agrobacterium-mediated transformation of Arabidopsis thaliana. Plant J. 1998:**16**(6):735–743. https://doi.org/10.1046/j.1365-313x. 1998.00343.x
- Curtis MD, Grossniklaus U. A gateway cloning vector set for highthroughput functional analysis of genes in planta. Plant Physiol. 2003:133(2):462–469. https://doi.org/10.1104/pp.103.027979
- **Eng RC, Wasteneys GO**. The microtubule plus-end tracking protein ARMADILLO-REPEAT KINESIN1 promotes microtubule catastrophe in Arabidopsis. Plant Cell. 2014:**26**(8):3372–3386. https://doi.org/10. 1105/tpc.114.126789
- Euteneuer U, McIntosh JR. Polarity of midbody and phragmoplast microtubules. J Cell Biol. 1980:87(2):509–515. https://doi.org/10.1083/jcb.87.2.509
- Gabel CA, Li Z, DeMarco AG, Zhang ZG, Yang J, Hall MC, Barford D, Chang LF. Molecular architecture of the augmin complex. Nature Commun. 2022:13(1):5449. https://doi.org/10.1038/s41467-022-33227-7
- **Grefen C, Donald N, Hashimoto K, Kudla J, Schumacher K, Blatt MR.**A ubiquitin-10 promoter-based vector set for fluorescent protein

- tagging facilitates temporal stability and native protein distribution in transient and stable expression studies. Plant J. 2010:**64**(2): 355–365. https://doi.org/10.1111/j.1365-313X.2010.04322.x
- Hamada T, Igarashi H, Itoh TJ, Shimmen T, Sonobe S. Characterization of a 200kDa microtubule-associated protein of tobacco BY-2 cells, a member of the XMAP215/MOR1 family. Plant Cell Physiol. 2004:45(9):1233–1242. https://doi.org/10.1093/pcp/pch145
- **Hashimoto T**. A ring for all: gamma-tubulin-containing nucleation complexes in acentrosomal plant microtubule arrays. Curr Opin Plant Biol. 2013:**16**(6):698–703. https://doi.org/10.1016/j.pbi.2013. 09 002
- Hotta T, Kong Z, Ho CM, Zeng CJ, Horio T, Fong S, Vuong T, Lee YR, Liu B. Characterization of the Arabidopsis augmin complex uncovers its critical function in the assembly of the acentrosomal spindle and phragmoplast microtubule arrays. Plant Cell. 2012:24(4):1494–1509. https://doi.org/10.1105/tpc.112.096610
- Hush JM, Wadsworth P, Callaham DA, Hepler PK. Quantification of microtubule dynamics in living plant cells using fluorescence redistribution after photobleaching. J Cell Sci. 1994:107(4):775–784. https:// doi.org/10.1242/jcs.107.4.775
- **Kawamura E, Wasteneys GO**. MOR1, the Arabidopsis thaliana homologue of Xenopus MAP215, promotes rapid growth and shrinkage, and suppresses the pausing of microtubules in vivo. J Cell Sci. 2008:**121**(24):4114–4123. https://doi.org/10.1242/jcs.039065
- **Kirik A, Ehrhardt DW, Kirik V.** TONNEAU2/FASS regulates the geometry of microtubule nucleation and cortical array organization in interphase Arabidopsis cells. Plant Cell. 2012:**24**(3):1158–1170. https://doi.org/10.1105/tpc.111.094367
- Kong Z, Hotta T, Lee YR, Horio T, Liu B. The {gamma}-tubulin complex protein GCP4 is required for organizing functional microtubule arrays in Arabidopsis thaliana. Plant Cell. 2010:22(1):191–204. https://doi.org/10.1105/tpc.109.071191
- Lampropoulos A, Sutikovic Z, Wenzl C, Maegele I, Lohmann JU, Forner J. GreenGate—a novel, versatile, and efficient cloning system for plant transgenesis. PLoS ONE. 2013:8(12):e83043. https://doi.org/10.1371/journal.pone.0083043
- **LeBlanc C, Zhang F, Mendez J, Lozano Y, Chatpar K, Irish VF, Jacob Y.** Increased efficiency of targeted mutagenesis by CRISPR/cas9 in plants using heat stress. Plant J. 2018:**93**(2):377–386. https://doi.org/10.1111/tpj.13782
- **Leong SY, Edzuka T, Goshima G, Yamada M**. Kinesin-13 and kinesin-8 function during cell growth and division in the moss Physcomitrella patens. Plant Cell. 2020;**32**(3):683–702. https://doi.org/10.1105/tpc. 19.00521
- Lindeboom JJ, Nakamura M, Hibbel A, Shundyak K, Gutierrez R, Ketelaar T, Emons AMC, Mulder BM, Kirik V, Ehrhardt DW. A mechanism for reorientation of cortical microtubule arrays driven by microtubule severing. Science. 2013:342(6163):1245533. https://doi.org/10.1126/science.1245533
- **Lipka E, Herrmann A, Mueller S**. Mechanisms of plant cell division. Wiley Interdiscip Rev Dev Biol. 2015:**4**(4):391–405. https://doi.org/10.1002/wdev.186
- Liu T, Tian J, Wang G, Yu Y, Wang C, Ma Y, Zhang X, Xia G, Liu B, Kong Z. Augmin triggers microtubule-dependent microtubule nucleation in interphase plant cells. Curr Biol. 2014:24(22):2708–2713. https://doi.org/10.1016/j.cub.2014.09.053
- Liu W, Zhu X, Lei M, Xia Q, Botella J, Zhu J, Mao Y. A detailed procedure for CRISPR/cas9-mediated gene editing in Arabidopsis thaliana. Sci Bull. 2015:60(15):1332–1347. https://doi.org/10.1007/s11434-015-0848-2
- Martin K, Kopperud K, Chakrabarty R, Banerjee R, Brooks R, Goodin MM. Transient expression in Nicotiana benthamiana fluorescent marker lines provides enhanced definition of protein localization, movement and interactions in planta. Plant J. 2009:59(1):150–162. https://doi.org/10.1111/j.1365-313X.2009.03850.x
- Murata T, Sano T, Sasabe M, Nonaka S, Higashiyama T, Hasezawa S, Machida Y, Hasebe M. Mechanism of microtubule array expansion

- in the cytokinetic phragmoplast. Nat Commun. 2013:4(1):1967. https://doi.org/10.1038/ncomms2967
- Murata T, Sonobe S, Baskin TI, Hyodo S, Hasezawa S, Nagata T, Horio T, Hasebe M. Microtubule-dependent microtubule nucleation based on recruitment of gamma-tubulin in higher plants. Nat Cell Biol. 2005:**7**(10):961–968. https://doi.org/10.1038/ncb1306
- Nagata T, Okada K, Takebe I, Matsui C. Delivery of tobacco mosaicvirus RNA into plant protoplasts mediated by reverse-phase evaporation vesicles (liposomes). Mol Gen Genet. 1981:184(2):161–165. https://doi.org/10.1007/BF00272899
- Obermann H, Mandelkow EM, Lange G, Mandelkow E. Microtubule oscillations—role of nucleation and microtubule number concentration. J Biol Chem. 1990:265(8):4382–4388. https://doi.org/10.1016/S0021-9258(19)39576-6
- Petry S, Groen AC, Ishihara K, Mitchison TJ, Vale RD. Branching microtubule nucleation in Xenopus egg extracts mediated by augmin and TPX2. Cell. 2013:152(4):768–777. https://doi.org/10.1016/j.cell. 2012.12.044
- Roostalu J, Cade NI, Surrey T. Complementary activities of TPX2 and chTOG constitute an efficient importin-regulated microtubule nucleation module. Nat Cell Biol. 2015:17(11):1422–1434. https://doi.org/10.1038/ncb3241
- Sasaki T, Fukuda H, Oda Y. CORTICAL MICROTUBULE DISORDERING1 is required for secondary cell wall patterning in Xylem vessels. Plant Cell. 2017:29(12):3123–3139. https://doi.org/10.1105/tpc.17.00663
- Sasaki T, Tsutsumi M, Otomo K, Murata T, Yagi N, Nakamura M, Nemoto T, Hasebe M, Oda Y. A novel katanin-tethering machinery accelerates cytokinesis. Curr Biol. 2019:29(23):4060–4070.e3. https://doi.org/10.1016/j.cub.2019.09.049
- Schiml S, Fauser F, Puchta H. CRISPR/Cas-mediated site-specific mutagenesis in Arabidopsis thaliana using cas9 nucleases and paired nickases. Methods Mol Biol. 2016:1469:111–122. https://doi.org/10.1007/978-1-4939-4931-1\_8
- Schindelin J, Arganda-Carreras I, Frise E, Kaynig V, Longair M, Pietzsch T, Preibisch S, Rueden C, Saalfeld S, Schmid B, et al. Fiji: an open-source platform for biological-image analysis. Nat Methods. 2012:9(7):676–682. https://doi.org/10.1038/nmeth.2019
- Schmidt S, Smertenko A. Characterization of a plant-specific microtubule-nucleating protein MACERATOR. Mol Biol Cell. 2016;27:3947–3947. https://doi.org/10.1091/mbc.e16-10-0736
- Schmidt S, Smertenko A. Identification and characterization of the land-plant-specific microtubule nucleation factor MACET4. J. Cell Sci. 2019:132:jcs232819. https://doi.org/10.1242/jcs.232819
- Seguié-Simarro JM, Austin JR, White EA, Staehelin LA. Electron tomographic analysis of somatic cell plate formation in meristematic cells of Arabidopsis preserved by high-pressure freezing. Plant Cell. 2004:16(4):836–856. https://doi.org/10.1105/tpc.017749
- Seguié-Simarro JM, Otegui MS, Austin JR II, Staehelin LA. Plant cyto-kinesis—insights gained from electron tomography studies. In: Verma DPS, Hong Z, editors. Plant cell monographs, cell division control in plants. Berlin, Heidelberg: Springer; 2008. p. 251–287.
- Shaner NC, Lambert GG, Chammas A, Ni YH, Cranfill PJ, Baird MA, Sell BR, Allen JR, Day RN, Israelsson M, et al. A bright monomeric green fluorescent protein derived from branchiostoma lanceolatum. Nat Methods. 2013:10(5):407–409. https://doi.org/10.1038/nmeth.2413
- **Shaw SL, Kamyar R, Ehrhardt DW**. Sustained microtubule treadmilling in Arabidopsis cortical arrays. Science. 2003:**300**(5626): 1715–1718. https://doi.org/10.1126/science.1083529
- Smertenko A, Moschou P, Zhang L, Fahy D, Bozhkov P. Characterization of cytokinetic mutants using small fluorescent probes. Methods Mol Biol. 2016:1370:199–208. https://doi.org/10.1007/978-1-4939-3142-2\_15
- Smertenko A, Hewitt SL, Jacques CN, Kacprzyk R, Liu Y, Marcec MJ, Moyo L, Ogden A, Oung HM, Schmidt S, et al. Phragmoplast

- microtubule dynamics—a game of zones. J Cell Sci. 2018:**131**(2): jcs203331. https://doi.org/10.1242/jcs.203331
- Smertenko AP, Chang HY, Wagner V, Kaloriti D, Fenyk S, Sonobe S, Lloyd C, Hauser MT, Hussey PJ. The Arabidopsis microtubule-associated protein AtMAP65-1: molecular analysis of its microtubule bundling activity. Plant Cell. 2004:16(8):2035–2047. https://doi.org/10.1105/tpc.104.023937
- Smertenko AP, Kaloriti D, Chang H-Y, Fiserova J, Opatrny Z, Hussey PJ. The C-terminal Variable region specifies the dynamic properties of Arabidopsis microtubule-associated protein MAP65 isotypes. Plant Cell. 2008:20(12):3346–3358. https://doi.org/10.1105/tpc.108.063362
- Smertenko AP, Piette B, Hussey PJ. The origin of phragmoplast asymmetry. Curr Biol. 2011:21(22):1924–1930. https://doi.org/10.1016/j.cub.2011.10.012
- Smertenko T, Turner G, Fahy D, Brew-Appiah RAT, Alfaro-Aco R, Engler JD, Sanguinet KA, Smertenko A. Brachypodium distachyon MAP20 functions in metaxylem pit development and contributes to drought recovery. New Phytol. 2020:227(6):1681–1695. https://doi.org/10.1111/nph.16383
- Song J-G, King MR, Zhang R, Kadzik RS, Thawani A, Petry S. Mechanism of how augmin directly targets the γ-tubulin ring complex to microtubules. J Cell Biol. 2018:217(7):2417–2428. https://doi.org/10.1083/jcb.201711090
- Steinert J, Schiml S, Fauser F, Puchta H. Highly efficient heritable plant genome engineering using cas9 orthologues from Streptococcus thermophilus and Staphylococcus aureus. Plant J. 2015:84(6):1295–1305. https://doi.org/10.1111/tpj.13078
- Sulimenko V, Dráberova E, Draber P. gamma-Tubulin in microtubule nucleation and beyond. Front Cell Dev Biol. 2022:10:880761. https://doi.org/10.3389/fcell.2022.880761
- **Thévenaz P, Ruttimann UE, Unser M**. A pyramid approach to subpixel registration based on intensity. IEEE Trans Image Process. 1998:**7**(1): 27–41. https://doi.org/10.1109/83.650848
- VanBuren V, Cassimeris L, Odde DJ. Mechanochemical model of microtubule structure and self-assembly kinetics. Biophys J. 2005:89(5):2911–2926. https://doi.org/10.1529/biophysj.105.060913
- Vyplelová P, Ovečka M, Komis G, Šamaj J. Advanced microscopy methods for bioimaging of mitotic microtubules in plants. Methods Cell Biol. 2018:145:129–158. https://doi.org/10.1016/bs.mcb.2018.03.019
- Walia A, Nakamura M, Moss D, Kirik V, Hashimoto T, Ehrhardt DW. GCP-WD mediates gamma-TuRC recruitment and the geometry of microtubule nucleation in interphase arrays of Arabidopsis. Curr Biol. 2014:24(21):2548–2555. https://doi.org/10.1016/j.cub.2014.09.013
- **Wasteneys GO**. Microtubule organization in the green kingdom: chaos or self-order? J Cell Sci. 2002:**115**(7):1345–1354. https://doi.org/10. 1242/ics.115.7.1345
- **Weigel D, Glazebrook J**. Arabidopsis: a laboratory manual. Cold Spring Harbor (N.Y.): Cold Spring Harbor Laboratory Press; 2002.
- Wieczorek M, Bechstedt S, Chaaban S, Brouhard GJ.
  Microtubule-associated proteins control the kinetics of microtubule
  nucleation. Nat Cell Biol. 2015:17(7):907–916. https://doi.org/10.
  1038/ncb3188
- Wu GK, Lin YT, Wei R, Chen YM, Shan ZY, Lee WH. Hice1, a novel microtubule-associated protein required for maintenance of spindle integrity and chromosomal stability in human cells. Mol Cell Biol. 2008:28(11):3652–3662. https://doi.org/10.1128/MCB.01923-07
- Yasuhara H, Sonobe S, Shibaoka H. Effects of taxol on the development of the cell plate and of the phragmoplast in tobacco BY-2 cells. Plant Cell Physiol. 1993;34(3):21–29. https://doi.org/10.1093/oxfordjournals.pcp.a078396
- Zhang LN, Smertenko T, Fahy D, Koteyeva N, Moroz N, Kuchařova A, Novák D, Manoilov E, Smertenko P, Galva C, et al. Analysis of formin functions during cytokinesis using specific inhibitor SMIFH2. Plant Physiol. 2021:186(2):945–963. https://doi.org/10.1093/plphys/kiab085